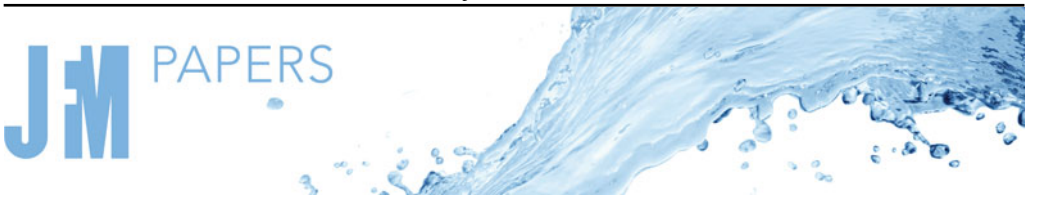
J. Fluid Mech. (2025), *vol.* 1013, A11, doi:10.1017/jfm.2025.10181



Electro-osmotic flow of semi-dilute polyelectrolyte solutions in nanochannels

Xinxi Liu[1], **Wenyao Zhang**[2], **Kai Jiao**[1], **Qiuwang Wang**[1] and **Cunlu Zhao**[1]

[1]MOE Key Laboratory of Thermo-Fluid Science and Engineering, School of Energy and Power Engineering, Xi'an Jiaotong University, Xi'an 710049, PR China

[2]PetroChina Shenzhen New Energy Research Institute Co., Ltd, Shenzhen 518063, PR China

Corresponding author: Cunlu Zhao, mclzhao@xjtu.edu.cn

(Received 22 July 2024; revised 22 July 2024; accepted 16 September 2024)

This paper presents a theoretical model for the electro-osmotic flow (EOF) of semi-dilute polyelectrolyte (PE) solutions in nanochannels. We use mean-field theories to describe the properties of electric double layer and viscosity of PE solutions that are prerequisites for constructing the EOF model. The EOF model is validated via a good match to the existing experimental results. Based on the validated EOF model, we conduct a comprehensive analysis of EOF of semi-dilute PE solutions in nanochannels. First, we observe considerable EOF of PE solutions in the uncharged nanochannels, which is in stark contrast to EOF of simple electrolyte solutions. The analyses show that the EOF of PE solutions in uncharged nanochannels is triggered by the external electric field acting on the near-wall non-electroneutral regions resulting from the confinement-induced inhomogeneous distribution of PE monomers. Although the solutions are electroneutral as a whole, the presence of local non-electroneutral regions and the mismatch between non-electroneutral regions and high-viscosity regions lead to the net EOF in uncharged nanochannels. Furthermore, we reveal that the EOF mobility μ_{eof} in uncharged nanochannels exhibits a scaling law $\mu_{eof} \propto a^{-0.44}$ (wherein a denotes monomer Kuhn length) and is inversely proportional to the PE chain length, while it decreases nonlinearly with the charge fraction of the PE chains. Moreover, the EOF mobility reaches its maximum at specific bulk monomer concentration, and increases with the nanochannel height before converging to that under no confinement. Second, we analyse the EOF of PE solutions in nanochannels with various wall effects, such as surface charge density, slip length and adsorption length. When the surface charge is absent, the adsorption length significantly influences the direction and magnitude of the EOF, whereas the slip length has no effect. When the wall becomes increasingly charged, the influence of adsorption length on EOF gradually diminishes, while the importance of the slip length progressively intensifies and the EOF is highly influenced by the co-action of various wall effects in a complicated manner. When the surface wall is oppositely charged to polymer

© The Author(s), 2025. Published by Cambridge University Press.

https://doi.org/10.1017/jfm.2025.10181 Published online by Cambridge University Press

monomers, the EOF mobility varies nonlinearly with the surface charge density, while a zero net flow of EOF followed by a direction reversal is discovered when the wall is likely charged to polymer monomers.

Key words: electrokinetic flows, polymers, microscale transport

1. Introduction

Electro-osmosis refers to the induced movement of a liquid through electrically charged porous materials when subjected to an external electric field (Bhattacharyya, Zheng & Conlisk 2005; Squires & Bazant 2006; Biscombe 2017). This electrokinetic process results in a net fluid motion, which is commonly known as electro-osmotic flow (EOF; see Gubbiotti *et al.* 2022). Over the past decades, extensive scholarly research has been conducted to investigate EOF in microchannels and nanochannels, and has given rise to a diverse range of practical applications such as fluid pumping (Ai *et al.* 2010), underground environmental remediation (Alshawabkeh, Yeung & Bricka 1999; Ma *et al.* 2020), nanopore sensing (Varongchayakul *et al.* 2018), biological delivery (Mondal & Shit 2017; Xu *et al.* 2021), blue energy harvesting (Siria, Bocquet & Bocquet 2017) and charged species transport across membranes or through porous media (Bondarev, Melnikov & Zabolotskiy 2023), to name a few.

Since the discovery of EOF in 1807 by Ferdinand Friedrich Reuss, studies have investigated extensively the EOF of simple electrolyte solutions inside micro/nanoscale channels and uncovered its characteristics (Vlassiouk, Smirnov & Siwy 2008; Zhao & Yang 2012; Feng *et al.* 2017; Alizadeh *et al.* 2021). More recently, in the past decade, the EOF of complex liquids has garnered tremendous attention due to its wide use in microfluidic devices that are widely expected to have a revolutionary impact on traditional chemical and biomedical analyses (Das & Chakraborty 2006; Tang *et al.* 2009; Zhao & Yang 2013; Xu *et al.* 2021). In particular, existing studies of EOF of complex liquids mostly assumed that the liquids obey certain types of non-Newtonian constitutive laws (Tang *et al.* 2009; Zhao & Yang 2013; Alizadeh *et al.* 2021), such as power law (Das & Chakraborty 2006; Zhao *et al.* 2008; Ng & Qi 2014; Hao *et al.* 2024), Carreau law (Ghosh, Chaudhury & Chakraborty 2016; Ko *et al.* 2019; Noreen *et al.* 2019; Ghiya & Tiwari 2024), Phan–Tien law (Martínez *et al.* 2016; Karan, Chakraborty & Chakraborty 2018; Sarma *et al.* 2018; Chen *et al.* 2019), Oldroyd-B law (Aziz, Mukarram & Kashif 2020; Panchun, Shaowei & Moli 2020; Ji, Qian & Liu 2021) or Casson law (Ng 2013; Murtaza *et al.* 2022; Srivally & Reza 2023). These works did not consider the microscopic details of non-Newtonian fluids, and considered that the liquids homogeneously obey the same non-Newtonian constative law in the entire flow domain. These treatments neglect the fact that non-Newtonian liquids are practically formed by dispersing particulate materials in Newtonian base liquids, and potentially become inhomogeneous under confinement (Li & Wu 2006; Jiang *et al.* 2018, 2019). The inhomogeneity in liquid properties would modify the EOF substantially, and this could be the reason why there is not yet a theoretical study that compares quantitatively well with the existing experiments.

The EOF pertaining to one special type of complex fluid, i.e. polyelectrolyte (PE) solutions, has received growing interest due to the unique properties of PEs (Manning 1978; Dobrynin & Rubinstein 2005; Yethiraj 2009; Lopez *et al.* 2017) as well as their diverse applications, such as colloid stability control, water treatment, biotechnology and energy engineering (Adachi & Xiao 2013; vander Straeten *et al.* 2017; DuChanois *et al.* 2019). A large fraction of the studies of PE-related EOF focused on cases in which the

https://doi.org/10.1017/jfm.2025.10181 Published online by Cambridge University Press

microchannel and nanochannel walls are grafted with PEs (Li *et al.* 2016; Bhattacharyya & Bag 2019; Li & Jian 2019; Roy, Bhattacharjee & De 2020; Sivasankar *et al.* 2021; Talebi, Ashrafizadeh & Sadeghi 2021), and such treatment leads to modifications of the surface charge density on the channel wall and then the EOF. The flowing media in these studies are still the simple electrolyte solutions.

Another category of EOF involving PEs concerns the use of the aqueous solutions of PEs as the flowing media in microchannels and nanochannels (Olivares, Vera-Candioti & Berli 2009; Uematsu & Araki 2013; Feng & Wong 2019; Bagchi & Olvera de la Cruz 2020). The EOF of PE solutions in microchannels and nanochannels has been relatively underexplored, potentially due to the complex nature and inhomogeneities of PE solutions under extreme confinement. The theoretical modelling of the EOF in these contexts requires the mathematical descriptions of both electric double layer (EDL) and viscous properties of solutions, which are straightforward for simple electrolyte solutions (Alizadeh *et al.* 2021). However, for PE solutions, accurate modelling of the EDL structure and viscous properties becomes challenging. This difficulty arises from the intricate interplay between the conformational and electrostatic properties of the PE solutions, and the significant absorption or depletion characteristics of PEs on channel walls (Uzum, Christau & von Klitzing 2011; Uezuem, Makuska & von Klitzing 2012). Moreover, unlike simple electrolytes, the application of an electric field has a much more significant impact on polymer solutions, such as the deformation of the depletion or adsorption layer, or the lift effect in the shear flow (Uematsu 2015; Perez Ocampo *et al.* 2022), hence making it harder to model the EOF system of PE solutions accurately.

Our comprehensive literature review indicates that characterisation of the EDL characteristics of PE solutions can be achieved via experiments, numerical simulation and theoretical modelling. Small-angle neutron scattering (Nierlich *et al.* 1985) and X-ray scattering (Combet, Lorchat & Rawiso 2012) have been used to observe the EDL of PE solutions. The characteritics of EDL detected by these techniques are averaged along the EDL thickness direction and cannot capture the inhomogeneous nature of EDL. Monte Carlo simulations (Woodward & Jonsson 1991; Carrillo & Dobrynin 2014) and molecular dynamics simulations (Gartner & Jayaraman 2019; Shen, Fan & Hall 2021) can reveal the EDL charateristics of PE solutions in extreme detail. However, they require significant computational resources and may be limited by the accuracy of the force fields used to describe the interactions between the components of the system. Theoretical methods such as mean-field theory (Jiao *et al.* 2022) and classical density functional theory (Jiang *et al.* 2018, 2019) have also been utilised to investigate the EDL structure of PE solutions. In particular, the mean-field theory is the most widely used theoretical approach to model the EDL of PE solutions because of its simplicity in concept and ability to characterise the major details of EDL structure (De Gennes *et al.* 1976; De Gennes 1982; Jiao *et al.* 2022).

The viscous properties of PE solutions are complicated by the conformational and electrostatic properties of polymer chains (Dobrynin, Colby & Rubinstein 1995; Lopez 2019; Dobrynin 2020; Matsumoto 2022). The studies of the viscous properties of PE solutions in the literature mainly focus on constructing various scaling laws. Fuoss first introduced the famous Fuoss's law based on a large amount of experimental data to describe the viscous properteis of semi-dilute PE solutions (Fuoss 1951; De Gennes *et al.* 1976). This empirical law features a scaling law $\eta \propto n_m^{1/2}$ in a salt-free environment, and a scaling law $\eta \propto n_m^{5/4}$ with added salts, where η represents the viscosity of the PE solution, and n_m represents the number of polymer monomers per volume. In addition to these scaling laws, more refined experiments (Lopez *et al.* 2015, 2017) found new scaling laws $\eta \propto n_m^{0.68}$ and $\eta \propto n_m^{0.91}$. In a more recent theoretical study, the mean-field theory was

https://doi.org/10.1017/jfm.2025.10181 Published online by Cambridge University Press

adopted to formulate a model that is able to recover all of the above empirical scaling laws (Chen, Perazzo & Stone 2020).

Although there have been theoretical models of EDL and viscous properties of PE solutions, the combination of the two to construct a accurate theoretical model of EOF has been absent, as is a theoretical model that quantitatively agrees with existing experiments. Hence in this study, we aim to formulate a theoretical model of EOF of semi-dilute PE solutions in nanochannels by combining the EDL and viscosity models of PE solutions derived from the mean-field approach. We first validate our EOF model by comparing our predictions with the experimental results (Olivares *et al.* 2009), then we employ our validated model to perform a comprehensive analysis of EOF of semi-dilute PE solutions in nanochannels, including the discovery of noticeable EOF in uncharged nanochannels, and the elucidation of various wall effects on the EOF characterisitics.

The paper is organised as follows. Section 2 is divided into two parts: the first part depicts the system that we considered and demonstrates the models of PE solutions as well as the SCFT (self consistent field theory) that we utilise in our work; the second part describes the governing equations of EOF in the system, and elaborates the model for describing the viscosity distribution of PE solutions. In § 3, we first validate our model with the experimental results, then demonstrate the generation of the EOF in semi-dilute PE solutions in uncharged nanochannels, and reveal the influence of various parameters on this counterintuitive EOF. Then we discuss various wall effects, including surface charge density, slip length and adsorption length, on the characteristics of EOF. Finally, we summarise the main findings and point out the direction for improving the current model in § 4.

2. Mathematical formulation

The system that we considered consists of two planar surfaces that form a slit nanochannel with height $2H$ and length L (here, $L/2H \gg 1$ and the end effect can be neglected); see figure 1. The slit nanochannel is filled with a semi-dilute aqueous solution of PE chains with salt added. The PE is negatively charged with a fixed charge fraction of f, and the polymerisation degree of each polymer chain is fixed at N_p (where $N_p \gg 1$). For simplicity, the salts in this work are symmetric $1:1$ simple electrolytes with bulk concentration c_s. And the cations are treated as identical to the counterions released by dissolved PEs. The solvent – which refers to water in this work– is treated as a continuum dielectric background with a uniform dielectric constant ϵ_w. Hence the components in the PE solution in figure 1 can be simply classified into three species, namely dissolved polyanions, small anions and small cations. Due to physicochemical reactions, the two nanochannel walls acquire surface charge density σ. Although the electrically neutral case (i.e. $\sigma = 0$) is considered as the main focus in this study, cases with negatively or positively charged surfaces have also been taken into consideration for comparative studies. In this work, the nanochannel has a sufficiently large length-to-height aspect ratio, namely, $L \gg 2H$. Therefore, the end effects can be neglected, and the original two-dimensional problem can be simplified to a one-dimensional problem along the channel height direction. All variables to be solved vary only along the z direction. Hence when an external electric field E is applied along the nanochannel surfaces in the x direction, an EOF is generated in the system and is governed by a simplified form of the Navier–Stokes equation (Uematsu & Araki 2013):

$$\frac{\mathrm{d}}{\mathrm{d}z}\left[\eta(z)\,\frac{\mathrm{d}v_x(z)}{\mathrm{d}z}\right] + \rho(z)\,E = 0, \tag{2.1}$$

https://doi.org/10.1017/jfm.2025.10181 Published online by Cambridge University Press

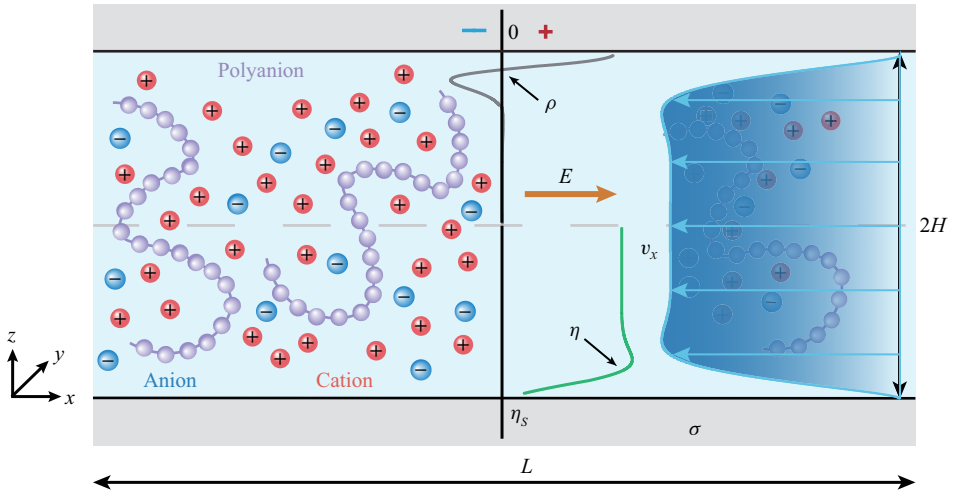


Figure 1. Schematic of a charged slit nanochannel filled with a PE solution. An electrical field E is applied along the slit nanochannel walls in the x direction. An EOF can occur in the system, with a possible velocity profile v_x shown graphically.

where $v_x(z)$ is the x component of the EOF field, and varies along the z axis only. From (2.1), one can observe that the EOF is jointly controlled by two factors, namely the local space charge density $\rho(z)$, and the local dynamic viscosity $\eta(z)$.

2.1. *Mean-field theory for EDL structure*

To describe the potential EOF in the system shown in figure 1, we should first have a knowledge of the EDL structure in the PE solution. Here, we adopt the mean-field theory to obtain the density profiles of each component in the PE solution system, which is a prerequisite for estimating the net charge density and the electric body force that the fluid experiences.

The essence of the theory is to establish an analytical expression for the total free energy $\mathcal{F}$ of the whole system. In this work, $\mathcal{F}$ can be written as the sum of three parts:

$$\mathcal{F} = \mathcal{F}_p(\boldsymbol{r}) + \mathcal{F}_i(\boldsymbol{r}) + \mathcal{F}_c(\boldsymbol{r}), \tag{2.2}$$

where $\boldsymbol{r}$ is the position vector in the system.

In (2.2), $\mathcal{F}_p(\boldsymbol{r})$ refers to the free energy contributed by polymer chains, and it can be further written as (Podgornik 1992; Borukhov, Andelman & Orland 1998; Shafir, Andelman & Netz 2003)

$$\beta\,\mathcal{F}_p(\boldsymbol{r}) = \int \mathrm{d}\boldsymbol{r}\,\frac{a^2}{6}|\,\nabla\phi(\boldsymbol{r})|^2 + \int \mathrm{d}\boldsymbol{r}\,\frac{\nu}{2}\left(\phi^4(\boldsymbol{r}) - \phi_b^4\right) - \beta\int \mathrm{d}\boldsymbol{r}\,\mu_p\left(\phi^2(\boldsymbol{r}) - \phi_b^2\right), \tag{2.3}$$

where $\beta = 1/k_BT$ represents the inverse of thermal energy, with k_B the Boltzmann constant, and T the absolute temperature of the system. Here, a is the intrinsic Kuhn length of the polymer chain, which can also be treated as the effective separation length of adjacent monomers; $\phi(\boldsymbol{r}) = \sqrt{c_b(\boldsymbol{r})}$ is the order parameter of local monomer concentration $c_b(\boldsymbol{r})$, which varies due to nano-confinement; $\phi_b = \sqrt{c_b}$, with c_b the monomer bulk concentration; ν is the second-virial coefficient characterising the excluded volume effect of polymer chains; μ_p is the chemical potential of the polymer. In (2.3), the

https://doi.org/10.1017/jfm.2025.10181 Published online by Cambridge University Press

three terms on the right-hand side come from the elastic energy, the excluded volume effect of the polymer chains, and the coupling with the bulk concentration, respectively.

In (2.2), $\mathcal{F}_i(\boldsymbol{r})$ refers to the free energy of the entropic contribution by small ions and their chemical potentials, which can be further written as (Podgornik 1992; Borukhov *et al.* 1998; Shafir *et al.* 2003)

$$\begin{aligned}\beta\mathcal{F}_i(\boldsymbol{r}) = &\int \mathrm{d}\boldsymbol{r}\,[c_+(\boldsymbol{r})\,(\ln(c_+(\boldsymbol{r})-1) - c_{+,b}(\ln(c_{+,b})-1)] - \beta\int \mathrm{d}\boldsymbol{r}\,\mu_+(c_+(\boldsymbol{r})-c_{+,b})\\ &+\int \mathrm{d}\boldsymbol{r}[c_-(\boldsymbol{r})\,(\ln(c_-(\boldsymbol{r})-1) - c_{-,b}(\ln(c_{-,b})-1)] - \beta\int \mathrm{d}\boldsymbol{r}\,\mu_-(c_-(\boldsymbol{r})-c_{-,b}),\end{aligned} \tag{2.4}$$

where $c_+(\boldsymbol{r})$ and $c_-(\boldsymbol{r})$ represent the local concentrations of small cations and anions, respectively, μ_+ and μ_- are the chemical potentials of small ions, respectively, and $c_{+,b}$ and $c_{-,b}$ are the bulk concentrations of small cations and small anions. In this system, $c_{-,b} = c_s$ and $c_{+,b} = f c_b + c_s$.

In (2.2), $\mathcal{F}_c(\boldsymbol{r})$ refers to the electrostatic free energy of the whole system, which can be further written as (Uematsu & Araki 2013; Jiao *et al.* 2022)

$$\beta\,\mathcal{F}_c(\boldsymbol{r}) = \beta\int \mathrm{d}\boldsymbol{r}\,\rho(\boldsymbol{r})\,\psi(\boldsymbol{r}) - \beta\int \mathrm{d}\boldsymbol{r}\,\frac{\epsilon_0\epsilon}{2}\,|\nabla\psi(\boldsymbol{r})|^2, \tag{2.5}$$

where $\rho(\boldsymbol{r}) = e[c_+(\boldsymbol{r}) - c_-(\boldsymbol{r}) - f\,\phi^2(\boldsymbol{r})]$ is the local net charge density, with e the elementary charge. Here, $\psi(\boldsymbol{r})$ is the local electrostatic potential, ϵ_0 is the vacuum permittivity, and ϵ is the relative permittivity of the PE solution. The relative dielectric permittivity of the solution is usually defined as (Nakamura 2018) $\epsilon = \sum \epsilon_i f_{vi}$, with ϵ_i and f_{vi} representing the relative dielectric permittivity and volume fraction of component i, respectively. In this study, the volume fraction of water ($\epsilon_w \sim 80$) is much larger than that of PE ($\epsilon_p \sim O(10)$). Hence the relative permittivity ϵ of the PE solution in this study is taken as that of water, ϵ_w, which is also a common practice in many previous theoretical and simulation studies (Carrillo & Dobrynin 2011; Gartner & Jayaraman 2019; Jiang, Ginzburg & Wang 2019; Bagchi & Olvera de la Cruz 2020; Jiang 2022).

After establishing the free energy of the system, one can obtain the thermodynamic equilibrium state of the system by minimising the free energy $\mathcal{F}$ with respect to $\phi(\boldsymbol{r})$, $c_+(\boldsymbol{r})$, $c_-(\boldsymbol{r})$ and $\psi(\boldsymbol{r})$. Note that in the slit nanochannel depicted in figure 1, all the physical properties can be considered to be variant only in the z direction. Hence by applying the variational method to $\mathcal{F}$ coupled with the neutral charge condition $c_{+,b} - c_{-,b} - f\phi_b^2 = 0$, one can obtain (see Appendix A)

$$\frac{a^2}{6}\frac{\mathrm{d}^2\phi}{\mathrm{d}z^2} = \nu\phi\left(\phi^2 - \phi_b^2\right) - f\phi\beta e\psi, \tag{2.6}$$

$$\beta e\frac{\mathrm{d}^2\psi}{\mathrm{d}z^2} = \kappa_s^2\sinh(\beta e\psi) - \kappa_p^2\left[\exp(-\beta e\psi) - \frac{\phi^2}{\phi_b^2}\right], \tag{2.7}$$

$$c_+(z) = \left(f\phi_b^2 + c_s\right)\exp(-\beta e\psi), \tag{2.8}$$

$$c_-(z) = c_s\exp(\beta e\psi), \tag{2.9}$$

where $\kappa_s = \sqrt{2\beta e^2 c_s/\epsilon_0\epsilon}$ and $\kappa_p = \sqrt{f\beta e^2 c_b/\epsilon_0\epsilon}$ are nominal Debye parameters associated with salt ions and PEs, respectively. Based on (2.6)–(2.9), the local space charge

https://doi.org/10.1017/jfm.2025.10181 Published online by Cambridge University Press

distribution $\rho(z)$ in (2.1) can be determined as

$$\rho(z) = ef\phi_b^2 \exp(-\beta e\psi) + 2ec_s \sinh(-\beta e\psi) - ef\phi^2, \tag{2.10}$$

which is a function of ψ and ϕ.

Equation (2.6) is the so-called Edward equation, and (2.7) is the modified Poisson–Boltzmann equation. Equations (2.6) and (2.7) jointly characterise the EDL near the surface walls. In this work, each monomer in a PE chain is assumed to uniformly carry $-fe$ fractional electric charge. This assumption leads to a simplified treatment of more realistic PE chains with randomly charged monomers (Dobrynin *et al.* 1995; Chen *et al.* 2020, 2021). The rationality of this assumption and the validity of our mean-field EDL model are validated via molecular dynamics simulations (see Appendix B).

2.2. *Mean-field theory for viscosity distribution*

In slit nanochannels, the viscosity of the PE solution $\eta(z)$ exhibits strong heterogeneity, and it is of significance to accurately characterise the distribution of $\eta(z)$ for EOF prediction. In this work, the characterisation of $\eta(z)$ is based on the model proposed by Chen, Perazzo & Stone (2021), which employs a mean-field approach to investigate how electrostatics of a semi-dilute PE solution contribute to the viscous properties of the untangled PE chains. As mentioned before, the PE chains are modelled as freely jointed flexible polymer monomers with polymerisation degree N_p. Each PE chain is uniformly charged with charge fraction f at equilibrium. On average, each polymer monomer carries charge fe, surrounded by small counterions of opposite charge that are packed into a so-called 'blob'. The concept of 'blob' was first introduced by De Gennes (1979) and further extended by Chen *et al.* (2021). As shown in figure 2, the PE chain is separated into successive blobs of size ς. Each blob has monomer concentration $c_{b,m}$ and salt concentration $c_{b,s}$. Hence each blob contains $g = c_{b,m}\varsigma^3$ monomers, and can be further divided into g closely packed monomers of size a. In this work, a is taken as the Kuhn length of the polymer chain.

Then the total free energy $\mathcal{F}_{blob}$ of a blob, which comprises an elastic component $\mathcal{F}_{els}$ and an electrostatic component $\mathcal{F}_{elec}$, can be given by (Chen *et al.* 2020, 2021)

$$\beta\mathcal{F}_{blob} = \beta(\mathcal{F}_{els} + \mathcal{F}_{elec}) = \frac{1}{a^2 c_{b,m}\varsigma} + \varsigma^3 f_{elec}(c_{b,m}, c_{b,s}, f), \tag{2.11a}$$

$$\beta\mathcal{F}_{els} = \frac{1}{a^2 c_{b,m}\varsigma}, \quad \beta\mathcal{F}_{elec} = \varsigma^3 f_{elec}(c_{b,m}, c_{b,s}, f), \tag{2.11b}$$

where $f_{elec}(c_{b,m}, c_{b,s}, f)$ represents the non-dimensional electrostatic energy density. Using extremisation of $\mathcal{F}_{blob}$ with respect to ς, based on the Zimm–Rouse model (De Gennes *et al.* 1976; Dobrynin *et al.* 1995; Chen *et al.* 2020), the relaxation time τ of N_p/g blobs on a PE chain can be given by

$$\tau = \beta\eta_s N_p^2 a^{1.5} c_{b,m}^{-1.25} f_{elec}^{0.75}, \tag{2.12}$$

where η_s is the viscosity of the solvent (water in our system). Moreover, the stress relaxation modules $G = c_{b,m}/(\beta N_p)$ and the viscosity $\eta = \tau G$ can be written as (Dobrynin *et al.* 1995)

$$\eta = \eta_s N_p \left(c_{b,m}a^3\right)^{0.5} \left(\frac{f_{elec}}{c_{b,m}}\right)^{0.75}. \tag{2.13}$$

https://doi.org/10.1017/jfm.2025.10181 Published online by Cambridge University Press

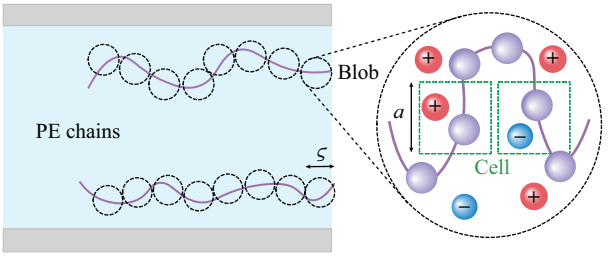


Figure 2. Schematic of the PE chain constructed by closely packed blobs of size ς that can be further divided into closed separated cells containing only one monomer of size a. Anions and cations exist in the solution to denote salt molecules.

Then by minimising $f_{elec}(c_{b,m}, c_{b,s}, f)$ and solving the nonlinear Poisson–Boltzmann equation, the various analytical expressions for η in different regimes of f and $c_{b,m}/c_{b,s}$ can be obtained as a function of $c_{b,m}$, $c_{b,s}$, f, a and N_p. The specific derivation is available in Chen *et al.* (2021) and will not be reiterated here. It is noted that in our study, (2.13) is applied locally along the channel height, with $c_{b,m}$ taking the value of $\phi^2(z)$. Since f, a and N_p are fixed and constant everywhere, the local viscosity distribution $\eta(z)$ can also be written as a function of ϕ and ψ, just like $\rho(z)$.

2.3. *Solution for EOF velocity distribution*

Integrating both sides of (2.1) and noting that the velocity satisfies the symmetric boundary condition on the centre plane (i.e. $(\mathrm{d}v_x(z)/\mathrm{d}z)|_{z=H} = 0$, we can obtain

$$\eta(z)\frac{\mathrm{d}v_x(z)}{\mathrm{d}z} = -\int_0^z \rho(z')\,E\,\mathrm{d}z' + \int_0^H \rho(z')\,E\,\mathrm{d}z'. \tag{2.14}$$

Note that the slit nanochannel walls bear a uniform charge density σ, and the whole system is constrained with an electroneutral condition that indicates

$$\int_0^H \rho(z')\,\mathrm{d}z' = -\sigma. \tag{2.15}$$

Integrating both sides of (2.14), and taking advantage of the Navier-slip boundary condition (El-Shehawy, El-Dabe & El-Desoky 2006; Bhagavatula & Castro 2007; Ferrás *et al.* 2012; Shojaeian & Koşar 2014; Misra & Sinha 2015) on the solid–solution interface, we have

$$v_x(0) = L_s\left.\frac{\mathrm{d}v_x(z)}{\mathrm{d}z}\right|_{z=0}, \tag{2.16}$$

where L_s is the Navier-slip length, and we can obtain the expression for $v_x(z)$ as

$$v_x(z) = v_x(0) - E\int_0^z \frac{\sigma + \int_0^{z_1}\rho(z_2)\,\mathrm{d}z_2}{\eta\,(z_1)}\,\mathrm{d}z_1. \tag{2.17}$$

Note that when $z = 0$, we can obtain from (2.14) and (2.16) that

$$v_x(0) = L_s\left.\frac{\mathrm{d}v_x(z)}{\mathrm{d}z}\right|_{z=0} = -L_s\frac{E\sigma}{\eta(0)}. \tag{2.18}$$

https://doi.org/10.1017/jfm.2025.10181 Published online by Cambridge University Press

Hence (2.17) can be rewritten as

$$v_x(z) = -L_s \frac{E\sigma}{\eta(0)} - E \int_0^z \frac{\sigma + \int_0^{z_1} \rho(z_2)\, \mathrm{d}z_2}{\eta\,(z_1)}\, \mathrm{d}z_1, \tag{2.19}$$

and the electro-osmotic mobility μ_{eof} can be calculated as

$$\begin{aligned}\mu_{eof} &= \frac{1}{2HE} \int_0^{2H} v_x(z)\, \mathrm{d}z \\ &= -\frac{1}{2H} \int_0^{2H} \left[L_s \frac{\sigma}{\eta(0)} + \int_0^z \frac{\sigma + \int_0^{z_1} (\rho(z_2))\ \mathrm{d}z_2}{\eta\,(z_1)}\, \mathrm{d}z_1 \right] \mathrm{d}z. \end{aligned} \tag{2.20}$$

As discussed before, $\eta(z)$ and $\rho(z)$ are both function of ψ and ϕ, and their distributions can be obtained by numerically solving the coupled equations (2.6) and (2.7) with the boundary conditions

$$\frac{1}{\phi}\frac{\mathrm{d}\phi}{\mathrm{d}z}\bigg|_{z=0} = \frac{1}{2D}, \quad \frac{\mathrm{d}\phi}{\mathrm{d}z}\bigg|_{z=H} = 0, \tag{2.21}$$

$$\frac{\mathrm{d}\psi}{\mathrm{d}z}\bigg|_{z=0} = -\frac{\sigma}{\epsilon_0 \epsilon}, \quad \frac{\mathrm{d}\psi}{\mathrm{d}z}\bigg|_{z=H} = 0. \tag{2.22}$$

Equations (2.21) give the Cahn boundary condition and the symmetric boundary condition in the channel centre. The Cahn boundary condition is first introduced by De Gennes (1982), with length D measuring the magnitude of the thickness of the adsorption layer. Thus the magnitude of D is inversely proportional to the van der Waals interaction between PEs and the surface wall. The surface wall is absorptive to the PEs when $D < 0$, and repulsive when $D > 0$. Equations (2.22) give the constant surface charge boundary condition at the wall and the symmetric boundary condition in the channel centre.

Applying the Simpson integration method to (2.19) and (2.20) based on the numerical results from (2.6) and (2.7), one can obtain the profile of EOF and all the physical properties that we need.

3. Results and discussion

3.1. *Validation of the model with the experiment*

We validate our model by comparing it with the experimental data reported by Olivares *et al.* (2009). The samples tested in the experiments are solutions of NaCMC and sodium dihydrogen phosphate (NaH_2PO_4). All the parameters are taken from Olivares *et al.* (2009) and Lopez *et al.* (2017), as shown in table 1. It is worth noting that when the sign of D is fixed, the specific value of D has minimal impact on the results at high σ, as the van der Waals forces between the PE and the surface become significantly smaller compared to the electrostatic forces. In the solution system under consideration, the PE is strongly charged and satisfies the condition $f_c < f < a/l_B$ proposed in Chen *et al.* (2021), with $f_c = a/\pi l_B$ the critical charge fraction, and $l_B = \beta e^2/4\pi\epsilon_0\epsilon$ the Bjerrum length. Here, $l_B \approx 0.7$ nm and $f_c \approx 0.29$. In our calculations, the local salt concentration is replaced by the local ionic strength $I(z) = 0.5(c_+ + c_-)$, and $\phi^2(z)/I(z)$ satisfies the condition $\phi^2(z)/I(z) \ll 2/f$ proposed in Chen *et al.* (2021). Under the defined regime of f and

https://doi.org/10.1017/jfm.2025.10181 Published online by Cambridge University Press

Parameters	a	f	N_p	c_s	c_b	D	ν	σ	H	T	ϵ
Values	0.65 nm	0.5	1900	8 mM	41 mM	0.2 nm	0.05 nm^3	-0.028 C m^{-2}	100 nm	298.15 K	80

Table 1. Values of key parameters in the calculation.

ϕ^2/I, expression of local viscosity $\eta(z)$ can be given by (Chen *et al.* 2021)

$$\frac{\eta(z)-\eta_s}{\eta_s} = N_p a^{1.5}\left(\frac{2}{f_c}\right)^{0.375}\left(\frac{f}{2}\right)^{1.5}\phi(z)^{1.75}\,I(z)^{-0.375}. \tag{3.1}$$

Figure 3(*a*) plots the experimentally measured data of electro-osmotic mobility μ_{eof} under various electric field strengths. The purple dashed and solid lines represent the theoretical predictions and experimental results from Olivares *et al.* (2009), respectively. It is noticeable that the theoretical predictions based on the power-law constitutive model with the experimentally determined rheological properties of bulk PE solutions significantly deviate from the experimental data even under micro-confinement (depicted by the purple solid line). This discrepancy implies the breakdown of macroscopic constitutive relations at the microscale and nanoscale. In contrast, our theoretical predictions, depicted by the solid blue line, show a close match to the experimental data with approximately 5 % error. It is also noticed that though demonstrating good accuracy, our model cannot predict the electric-field-strength-dependent characteristics of EOF mobility observed in the experiment. The reason for this could be that the viscosity model used in the current work was derived under the condition of zero shear rate and is shear-independent. Figure 3(*b*) illustrates the model-predicted velocity profile of the EOF, revealing a plug-like profile extending swiftly from the channel walls to the bulk value in the central channel. Equation (2.1) implies that the EOF is governed jointly by the local charge density $\rho(z)$ and the local viscosity $\eta(z)$ distribution, which are depicted in figures 3(*c*) and 3(*d*), respectively. Cations accumulate near the surface wall due to electrostatic attraction, while anions and monomers are depleted due to electrostatic repulsion and van der Waals forces (figure 3*e*), which gives rise to the peak value of net charge density at the surface wall. Moreover, as the local ionic strength $I(z)$ diminishes and the PE concentration $\phi^2(z)$ rises (figure 3*e*), $\phi^2(z)/I(z)$ escalates incrementally, prompting a rapid elevation in local viscosity $\eta(z)$ (figure 3*d*). Notably, our viscosity model is applicable only within the semi-dilute regime and significantly underestimates actual values within the entangled regime. However, this discrepancy does not affect our predictive outcomes since viscosity outside the EDL does not influence the development of EOF and our model is able to effectively capture the physical properties within the double layer. Figure 3(*f*) represents the dimensionless electric potential distribution $\beta e\psi$, and a reversal of $\beta e\psi$ is observed at a short distance from the surface wall, which is the so-called overcharging potential.

3.2. *EOF in uncharged nanochannels*

The reliability of our model has been validated through comparison with experimental data. In this subsection, we use the established model to investigate the EOF behaviour of semi-dilute salt-free PE solutions confined within neutral nanochannels (i.e. $\sigma = 0$), and carry out a series of parametric studies. Note that when the PE solution is considered as

https://doi.org/10.1017/jfm.2025.10181 Published online by Cambridge University Press

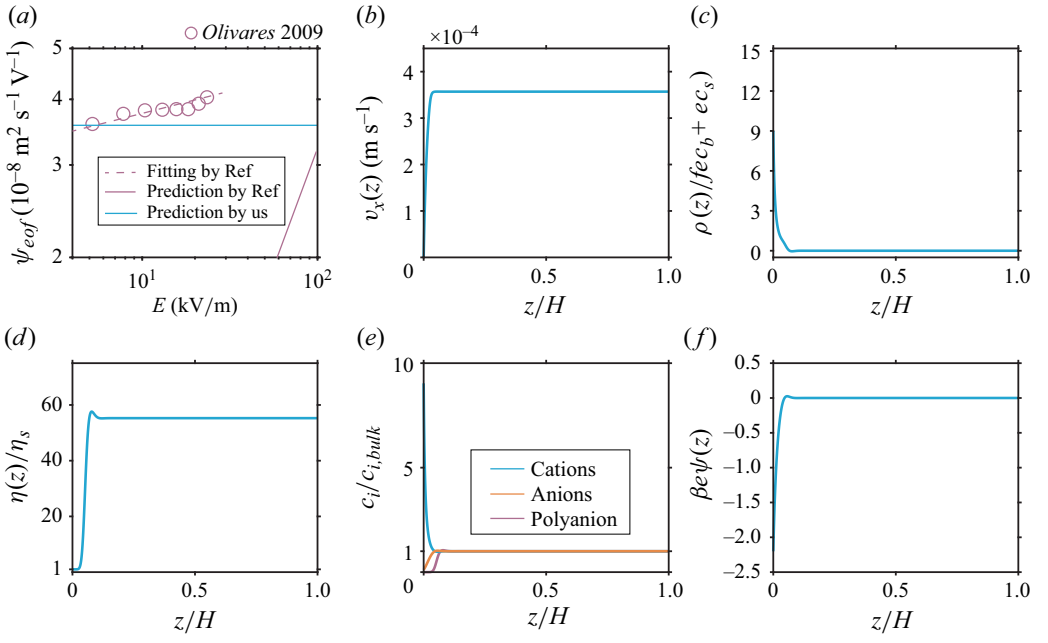


Figure 3. Validation of the EOF model with the experiment by Olivares *et al.* (2009). (*a*) Comparison of experimental EOF mobility with those predicted by theoretical models. (*b*) The EOF velocity profile. (*c*) Space charge density profile. (*d*) Viscosity distribution profile. (*e*) Polyanions and small ions density profile normalised by respective bulk value. (*f*) Electric potential distribution profile.

salt-free, an approximation of $\eta(z)$ can be given by (Chen *et al.* 2021)

$$\frac{\eta(z)-\eta_s}{\eta_s} = N_p(\phi^2(z)\,a^3)^{0.5}\left[f\,\sinh^{-1}\left(0.5f\frac{\phi^2(z)}{c_s(z)}\right)\right]^{0.75}. \tag{3.2}$$

For salt-free cases, $c_s(z)$ can be redefined as $c_s(z)=\alpha\,\phi^2(z)+\lambda$, where α represents the proportion of the residual of salt carried by PEs, and λ represents the salt left behind from contamination in the solvent. Here, for highly pure PE solutions with no salt added, α is fixed at 0.001 and λ is fixed at 10^{-8} M (Chen *et al.* 2020). After replacing $c_s(z)$ with $\alpha\,\phi^2(z)+\lambda$, (3.2) can be rewritten as

$$\frac{\eta(z)-\eta_s}{\eta_s} = N_p(\phi^2(z)\,a^3)^{0.5}\left[f\,\sinh^{-1}\left(0.5f\frac{\phi^2(z)}{\alpha\,\phi^2(z)+\lambda}\right)\right]^{0.75}. \tag{3.3}$$

We aim to demonstrate the emergence of an unconventional EOF in uncharged nanochannels under an external electric field $E=100\ \mathrm{V\ cm^{-1}}$. The PE solution has bulk monomer density 0.1 M, and the polymerisation degree of a polymer chain is $N_p=200$, with charge fraction $f=0.5$. The Kuhn length of the polymer chain is set at $a=0.5$ nm, and the adsorption length is $D=0.2$ nm. The absolute temperature is kept at $T=300$ K, with $\epsilon=80$. The height of the slit nanochannel is fixed at $2H=10$ nm, and the Navier-slip length is set as $L_s=0$ (i.e. the no-slip boundary condition).

Figure 4(*a*) presents the profile of reduced EOF velocity $v_x(z)/v_{ref}$, with $v_{ref}=1\ \mu\mathrm{m\ s^{-1}}$ the reference velocity, and shows that a considerable EOF is generated in the direction opposite to the x axis. As is discussed, the EOF in our system is controlled by $\rho(z)$ and $\eta(z)$ depicted in figures 4(*b*) and 4(*c*), respectively. From figure 4(*d*) we can find that the negatively charged monomers are depleted in the near-wall region due to the

https://doi.org/10.1017/jfm.2025.10181 Published online by Cambridge University Press

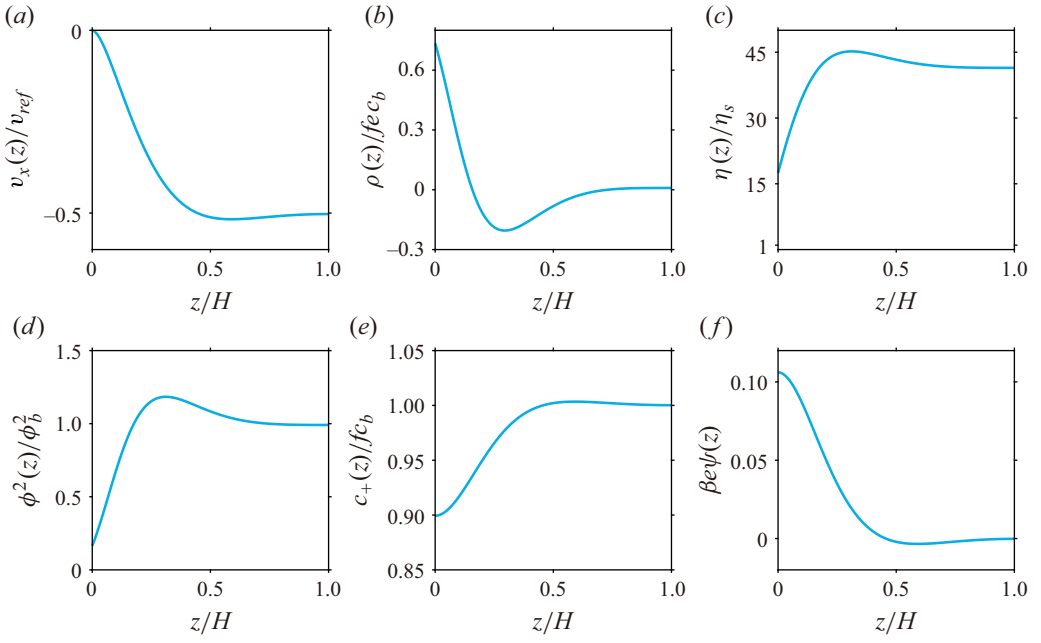


Figure 4. The EOF of a PE solution in an uncharged nanochannel. (*a*) The EOF velocity profile. (*b*) Space charge density profile. (*c*) Viscosity distribution profile. (*d*) Monomer density profile. (*e*) Counterion density profile. (*f*) Electric potential distribution profile.

conformational entropy of the PE chains and the van der Waals repulsion from the surface wall. The counterions (i.e. the small cations) are also depleted in the near-wall region, but to a much less degree (figure 4*e*). We can also observe that the concentration of the monomers $\phi(z)^2$ increases rapidly and reaches an absorption peak larger than its bulk value (i.e. ϕ_b^2) before levelling off to the bulk. This can be attributed to the electrostatic attraction from oppositely charged counterions and the constraint of electroneutrality in the entire system. Consequently, the distinct density distributions of polyanions and positively charged counterions result in an EDL structure with a non-zero net space charge density in the near-wall region of the nanochannel, as shown in figure 4(*b*). As expected, net positive charges accumulate near the channel walls (figure 4*b*), followed by a sharp transition to net negative charges, reaching a minimum. This behaviour exhibits a pronounced oscillation with a decaying amplitude and alternating signs. With the application of the external electric field, the dramatic fluctuations of $\rho(z)$ exert electric body forces, which contribute to the generation of EOF.

From figure 4(*a*), we can find that the EOF occurs in the opposite x direction despite a relatively large positive electric body force acting near the two channel walls, which can be ascribed to the fact that a larger portion of the central nanochannel region bears a negative electric body force and dominates the EOF. This phenomenon aligns with the traditional Helmholtz–Smoluchowski equation ($-\epsilon_0\epsilon\psi_S/\eta_0$). Despite the zero surface charge density, the charge separation induced by nano-confinement gives rise to a certain positive electrostatic potential on the surface wall (figure 4*f*) and results in an EOF in the negative x direction. Another intriguing phenomenon is discovered that under this unconventional EOF, the velocity gradient at the wall equals zero (figure 4*a*), which implies that the EOF remains independent of the Navier-slip length L_s in (2.16). We can also observe that the magnitude of the EOF velocity surges to a peak, then tardily declines

https://doi.org/10.1017/jfm.2025.10181 Published online by Cambridge University Press

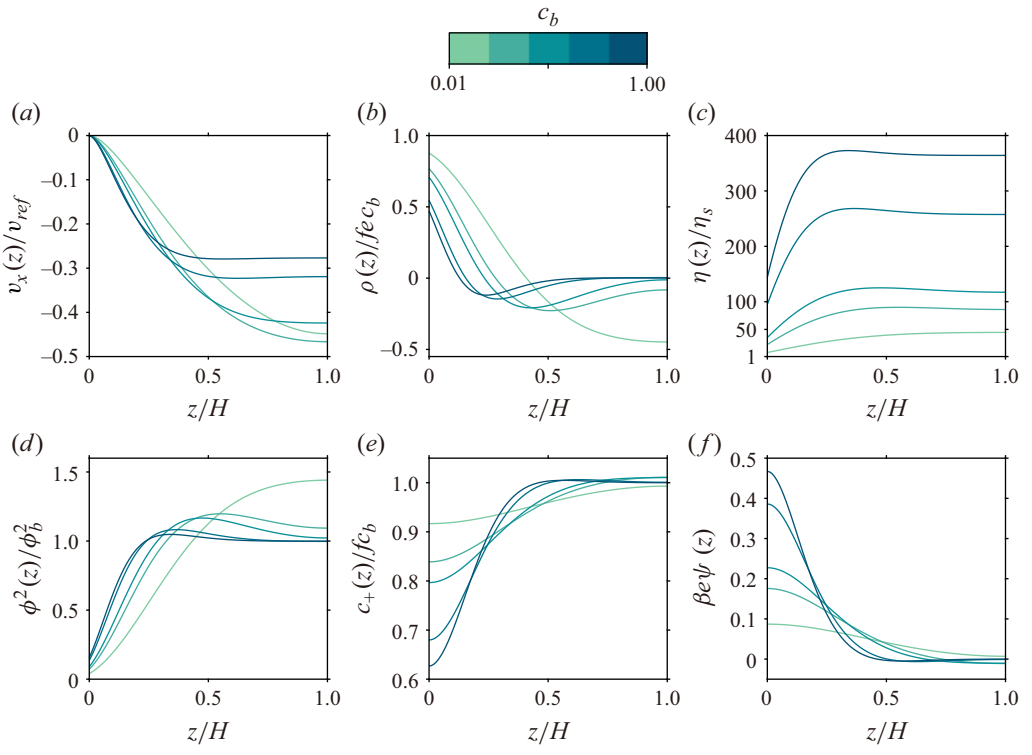


Figure 5. Dependence of EOF on bulk monomer density c_b. (*a*) The EOF velocity profile. (*b*) Space charge density profile. (*c*) Viscosity distribution profile. (*d*) Monomer density profile. (*e*) Counterion density profile. (*f*) Electric potential distribution profile. The PE solution consists of only one type of polymer, with $N_p = 200$, $f = 0.5$, $a = 1$ nm, $H = 5$ nm, $D = 0.2$ nm, and c_b varies among 0.01, 0.05, 0.1, 0.5 and 1.0 M.

to a constant value slightly lower than the peak (figure 4*a*). This unique profile of the EOF is due to the net charge density oscillation induced by ionic layering, along with the competition effect between electric body forces and the hindrance effect from viscosity. From figure 4(*c*), we can observe that the reduced viscosity shares a similar trend with the reduced monomer concentration, which exerts a relatively small obstruction on the flow near the channel wall, and stabilises the EOF in the central region.

So far, we have elucidated the origin of an appreciable EOF of PE solutions in a nanochannel with neutral walls. The following subsubsections investigate the influence of various factors on this unconventional EOF.

3.2.1. *Effect of monomer bulk concentration on EOF*

We first examine the influence of the monomer bulk concentration c_b on the EOF, by considering a typical strongly charged PE with $f = 0.5$ at various c_b values. From figure 5(*a*), we can observe that at high c_b, the magnitude of EOF velocity surges to a peak value and displays a plug-like profile. However, this behaviour is delayed at lower c_b values, as the EOF magnitude grows more slowly and the plateau region at the centre of the nanochannel becomes shorter. Furthermore, when the monomer bulk concentration falls below 0.1 M, the plateau almost disappears and the EOF shifts to a parabolic-like shape. It is also observed that the central flow velocity of the EOF undergoes an obvious nonlinear change, initially increasing and then gradually decreasing as c_b increases. This nonlinear variation is attributed to the combined influence of $\rho(z)$ and $\eta(z)$ as depicted

https://doi.org/10.1017/jfm.2025.10181 Published online by Cambridge University Press

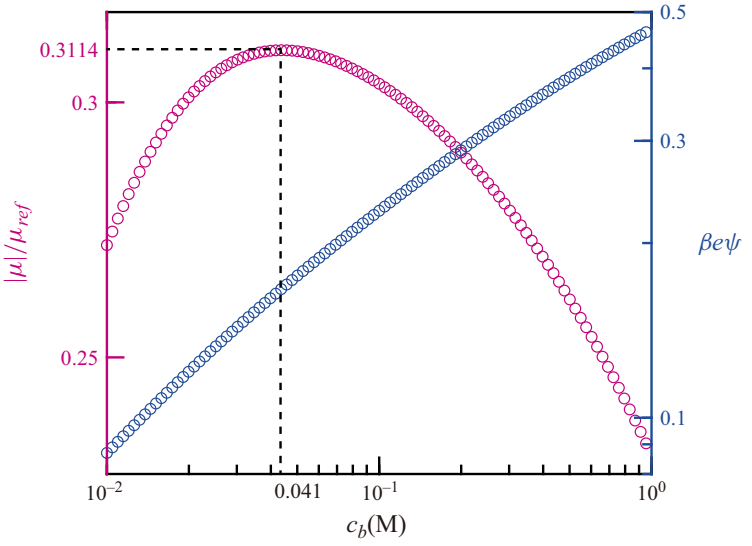


Figure 6. Reduced electro-osmotic mobility and non-dimensional induced zeta potential as a function of monomer bulk concentration c_b.

in figures 5(*b*) and 5(*c*), respectively. Figure 5(*d*) illustrates that due to decreased osmotic pressure with the decrease of c_b, polymer monomers are depleted deeper at the surface wall at a broader range with a higher absorption peak. In contrast, counterions are less depleted at low c_b (figure 5*e*). Therefore, as PE solutions become more dilute, the oscillation of net charge density gets broader along with a more pronounced magnitude (figure 5*b*). This also suggests the expansion of the EDL thickness in the solution, which accounts for the shift of density profile of the EOF when the two EDLs start to overlap. As c_b increases, the alterations in the double layer thickness are also evident in figure 5(f). It is noticeable that the induced positive surface zeta potential intensifies at higher c_b and diminishes to zero within a more narrow range.

As c_b rises, the ionic strength of the solution increases, and intensifies the electric field forces acting on the system. However, this amplification is counteracted by the escalating viscosity of the solution. Figure 5(*c*) illustrates that $\eta(z)$ increases at higher c_b, hindering the conduction of electric field forces, and further impeding the development of EOF. In this interplay of competing influences, the EOF mobility demonstrates a nonlinear variation, further highlighted in figure 6 with $\mu_{ref} = 10^{-10}$ m^2 V^{-1} s^{-1} the reference electro-osmotic mobility. As the induced zeta potential continues to increase with rising c_b, the EOF mobility shows a nonlinear trend, reaching an extremum at monomer bulk concentration approximately 0.041 M. This nonlinear variation (figures 5(*a*) and 6) is a consequence of the competitive effect between the electric field forces and viscosity of the PE solution. Moreover, the induced zeta potential ψ is found to increase nonlinearly with c_b (figure 6).

3.2.2. *Effect of polymer charge fraction on EOF*

We then investigate the effects of the polymer charge fraction f on the reported EOFs. As stated previously, we use a mean-field approach and assume that each monomer carries fractional charge fe for a polymer chain with charge fraction f at equilibrium. In this subsubsection, the Kuhn length of the polymer chain is fixed at $a = 1.0$ nm, hence the critical charge fraction is defined as $f_c \approx 0.45$ (Chen *et al.* 2020, 2021). In order to provide

https://doi.org/10.1017/jfm.2025.10181 Published online by Cambridge University Press

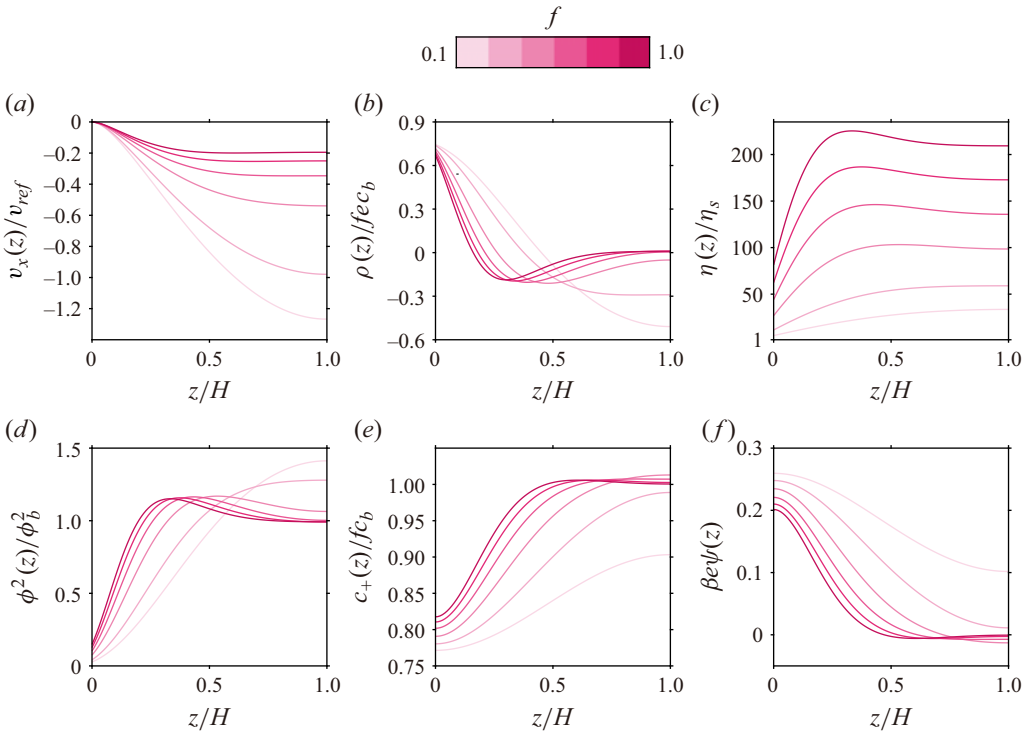


Figure 7. Dependence of EOF on polymer charge fraction f. (*a*) The EOF velocity profile. (*b*) Space charge density profile. (*c*) Viscosity distribution profile. (*d*) Monomer density profile. (*e*) Counterion density profile. (*f*) Electric potential distribution profile. The PE solution consists of only one type of polymer, with $N_p = 200$, $c_b = 0.1$ M, $a = 1$ nm, $H = 5$ nm, $D = 0.2$ nm, and f varies among 0.1, 0.2, 0.4, 0.6, 0.8 and 1.0.

a more comprehensive assessment, both strongly charged cases (i.e. $f < f_c$) and weakly charged cases (i.e. $f > f_c$) have been taken into consideration.

Figure 7(*a*) plots the EOF velocity profiles for various f values. It can be observed that as the charge fraction f of the polymer chain increases, the PE transitions from a weakly charged state to a strongly charged state, leading to a concurrent weakening of the EOF. Additionally, the EOF gradually shifts from a parabolic-like profile at low f to a plug-like profile at high f. In particular, the EOF velocity rises more gradually from the surface wall to the channel centre, reaching a lower maximum value within a broader region. This variation of $v_x(z)$ is attributed to the combined influence of $\rho(z)$ and $\eta(z)$ as depicted in figures 7(*b*) and 7(*c*), respectively. Figure 7(*d*) illustrates that with the decrease of f, polymer monomers are depleted deeper at the surface wall at a broader range with a higher absorption peak. Counterions are also more depleted at low f (figure 7*e*). We note that both $\phi^2(z)$ and $c_+(z)$ do not revert to their respective bulk concentration in the centre of the nanochannel. This phenomenon arises when the PE is weakly charged and behaves more like a neutral polymer, which leads to a lower ionic strength within the solution and hence results in an increase in the thickness of the EDL. Under nano-confinement in this study, this change leads to the overlap of the EDLs on both wall surfaces, consequently altering the central region of the channel, which no longer retains the physical properties of the bulk solution. Therefore, as the PE becomes more strongly charged, the oscillation of net charge density ρ shrinks along with a less pronounced magnitude (figure 7*b*), which accounts for the shift of density profile with varying f (figure 7*a*). The alteration of EDLs

https://doi.org/10.1017/jfm.2025.10181 Published online by Cambridge University Press

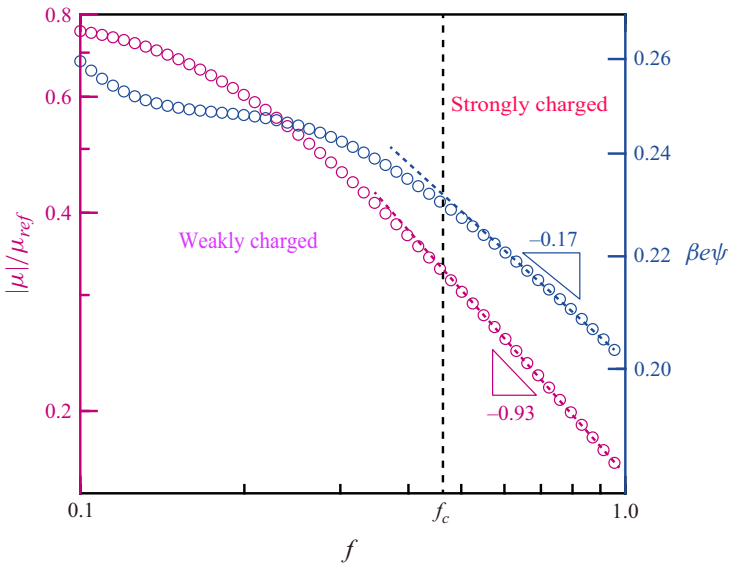


Figure 8. Reduced electro-osmotic mobility and non-dimensional induced zeta potential as functions polymer charge fraction f, where the critical charge fraction here is $f_c = 0.45$.

is also reflected in figure 7(f): as f increases, the induced positive surface zeta potential slightly decreases and diminishes to bulk value within a more narrow range.

At low f, the net charge density in the EDL is reduced and leads to the decrease in the electric body forces acting on the PE solution. Nevertheless, the decline in this propelling force is counteracted by the viscous effect. As seen in figure 7(d), in most regions of the EDL where the EOF evolves, both $\phi^2(z)$ and f are relatively low in comparison to values at higher f. Consequently, based on (3.3), there is a considerable reduction in local viscosity in the EDL when PEs are weakly charged (figure 7c). This diminishing viscosity paradoxically leads to an incremental strengthening of EOF as it predominates over electric body force effect at low f (figure 7a).

Figure 8 plots how μ_{eof} and ψ vary with f, and is divided into two regions based on the critical charge fraction f_c, with the left-hand side representing the scenario of weakly charged PEs, and the right-hand side depicting the strongly charged ones. We can notice that when $f < f_c$, both μ_{eof} and ψ exhibit a nonlinear decline with f. Conversely, upon f surpassing f_c, the EOF mobility and the induced zeta potential tend to decrease consistently with f. After fitting the scatter data on a logarithmic scale, two scaling laws, $\mu_{eof} \propto f^{-0.93}$ and $\psi \propto f^{-0.17}$, are reported. It is noteworthy that the scaling exponent of μ_{eof} with respect to f is exactly the reciprocal of the scaling exponent of viscosity with respect to f in the viscosity model proposed by Chen *et al.* (2020). This implies that μ_{eof} is significantly influenced by f when the polymer chain is strongly charged.

3.2.3. *Effect of monomer Kuhn length on EOF*

We next investigate the effects of the monomer Kuhn length a on the reported EOFs. Equation (2.6) illustrates that a reflects the rigidity of a polymer and hence influences the elastic energy of the chain. In this subsubsection, the EOFs of various a ($a = 0.5$, 0.6, 0.7, 0.8, 0.9, 1.0 nm) are studied. It is noted that PEs are endowed with a fixed charge fraction $f = 0.5$, which is larger than the critical charge fraction $f_c = a/\pi l_B$. This means that all PEs are strongly charged.

https://doi.org/10.1017/jfm.2025.10181 Published online by Cambridge University Press

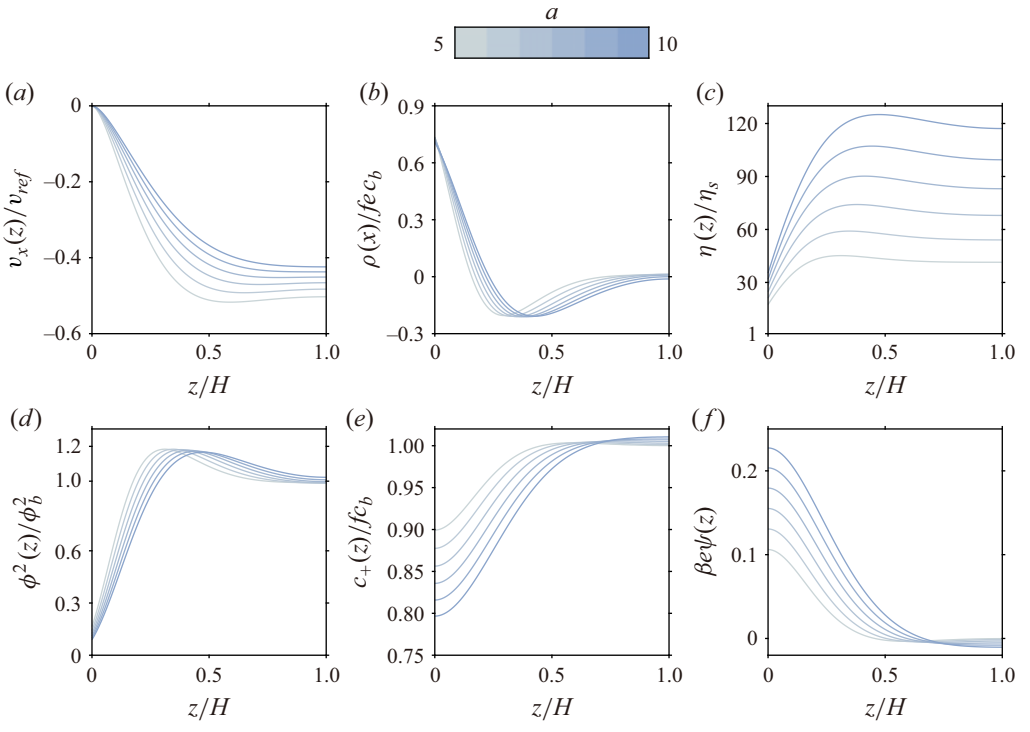


Figure 9. Dependence of EOF on polymer Kuhn length a. (a) The EOF velocity profile. (b) Space charge density profile. (c) Viscosity distribution profile. (d) Monomer density profile. (e) Counterion density profile. (f) Electric potential distribution profile. The PE solution consists of only one type of polymer, with $N_p = 200$, $c_b = 0.1$ M, $f = 0.5$, $H = 5$ nm, $D = 0.2$ nm, and a varies among 0.5, 0.6, 0.7, 0.8, 0.9 and 1.0 nm.

Figure 9(a) plots the EOF velocity profiles for various monomer Kuhn lengths a. We can observe that at smaller a, the EOF is enhanced, with EOF profile shifting from the plug-like shape to an obvious W-like shape. This variation of $v_x(z)$ is attributed to the combined influence of $\rho(z)$ and $\eta(z)$ as depicted in figures 9(b) and 9(c), respectively. Figure 9(d) illustrates that when a increases, polyanions are more depleted at the surface wall due to increasing penalty of conformational entropy. The depletion length of polyanions is also broaden, which is affected by the correlation length of semi-dilute PE solution $\xi \sim O(a)$. The augmented $\phi^2(z)$ in the vicinity of surface walls leads to the increased concentration of counterions due to electrostatic attraction (figure 9e). Interestingly, the variations of $\phi^2(z)$ and $c_+(z)$ share trends similar to those depicted in figures 7(d) and 7(e). This can be explained by the fact that the variation of a implies the alteration of charge fraction f. At small a, the Kuhn length between PE segments is decreased, thereby lowering the threshold of being strongly charged (i.e. f_c declines). When the polymer chain is endowed with a fixed charge fraction, an increase in Kuhn length reduces the relative electrification; in other words, it decreases the charge fraction f. Hence at smaller a, a more pronounced oscillation of net charge density ρ (figure 7b) is observed, which results in the W-like shaped EOF profile (figure 7a). For different Kuhn lengths, variations in net charge density ρ are minor, hence the magnitude of EOFs is governed primarily by the viscous effects. Figure 7(c) illustrates that the viscosity within the EDL increases at larger a, thereby impeding the EOF flow. Figure 7(f) demonstrates the induced zeta potential at the surface walls, where significant overcharging is observed at large a.

https://doi.org/10.1017/jfm.2025.10181 Published online by Cambridge University Press

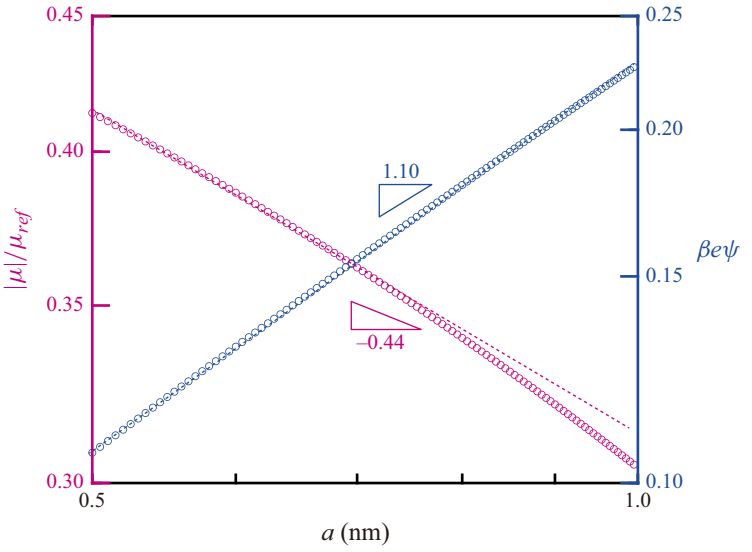


Figure 10. Reduced electro-osmotic mobility and non-dimensional induced zeta potential as functions of polymer Kuhn length a.

Figure 10 plots how μ_{eof} and ψ vary with a. After fitting the scatter data on a logarithmic scale and ensuring that the error between the scatter data and the predicted data is less than 5 %, we can notice that both μ_{eof} and ψ exhibit a power-law relationship with a, and two scaling laws, $\mu_{eof} \propto a^{-0.44}$ and $\psi \propto a^{1.10}$, are reported. This illustrates that although the zeta potential increases as a increases, the actual EOF mobility decreases due to the significant effect on the viscosity brought by a, thereby curtailing the velocity.

3.2.4. *Effect of polymer polymerisation degree on EOF*

In this subsubsection, we probe into how polymerisation degree of PE chains N_p influences the EOF. It is worth mentioning that in this work, we consider only cases with $N_p \gg 1$, which means that the translational entropy of the polymers can be neglected (i.e. $\int \mathrm{d}\boldsymbol{r}\ (\phi^2/N_p)(\ln \phi^2 - 1)$). Hence the polymerisation degree N_p exerts no effect on the EDL structure in our calculations. This approach is rational because the ion concentration in the semi-dilute PE solutions is sufficiently high so that ξ is insensitive to the polymer chain length and is determined mainly by electrostatic interactions among ions. From figure 11, we can observe that profiles of $\rho(z)$, $\phi^2(z)$, $c_+(z)$ and ψ look identical, which is also verified by classical density functional theory (Jiang *et al.* 2019). Hence the EOF (figure 11*a*) is determined by viscosity with varying N_p. When other parameters are fixed, the local viscosity is dependent only on N_p (figure 11*c*), and figure 12 illustrates that the EOF mobility is inversely proportional to the polymerisation degree N_p, which gives $\mu_{eof} \propto N_p^{-1}$.

3.2.5. *Effect of nanochannel height on EOF*

We next investigate the effects of nanochannel height $2H$ on the reported EOFs. A dimensional parameter $2H\kappa$ is utilised to characterise the confinement degree of PE solutions in the slit nanochannel, where $\kappa^{-1} \approx 2$ nm, with other parameters held constant. The degree of confinement weakens as $2H\kappa$ increases. As $2H\kappa$ approaches 1, the system is considered highly constrained, whereas a $2H\kappa$ value exceeding 5 indicates

https://doi.org/10.1017/jfm.2025.10181 Published online by Cambridge University Press

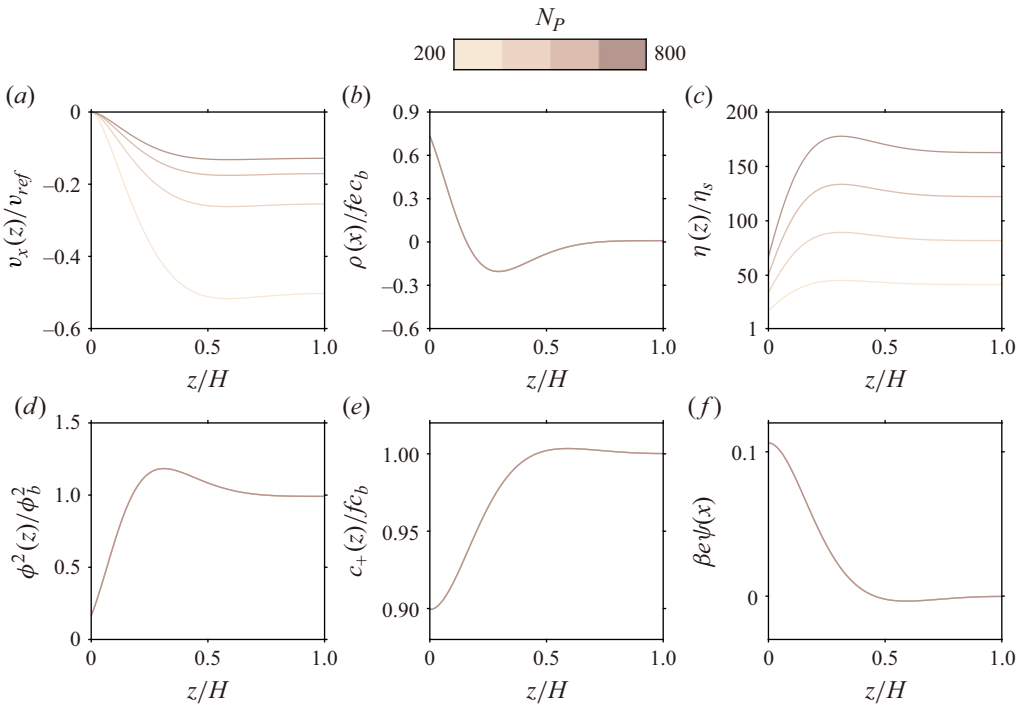


Figure 11. Dependence of EOF on polymer polymerisation degree N_p. (*a*) The EOF velocity profile. (*b*) Space charge density profile. (*c*) Viscosity distribution profile. (*d*) Monomer density profile. (*e*) Counterion density profile. (*f*) Electric potential distribution profile. The PE solution consists of only one type of polymer, with $a = 1.0$ nm, $c_b = 0.1$ M, $f = 0.5$, $H = 5$ nm, $D = 0.2$ nm, and N_p varies among 200, 400, 600 and 800.

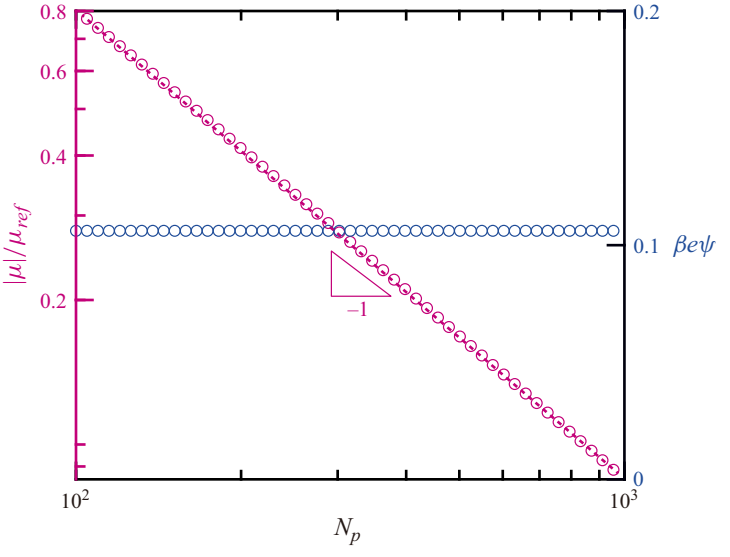


Figure 12. Reduced electro-osmotic mobility and non-dimensional induced zeta potential as functions of polymer polymerisation degree N_p.

https://doi.org/10.1017/jfm.2025.10181 Published online by Cambridge University Press

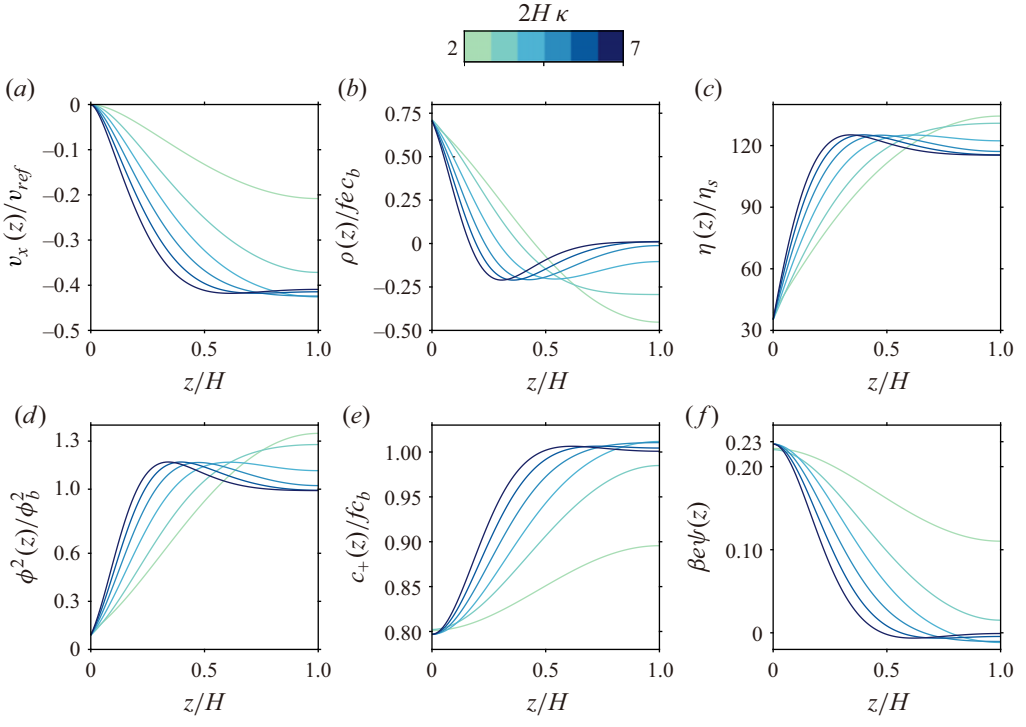


Figure 13. Dependence of EOF on nanochannel height H. (*a*) The EOF velocity profile. (*b*) Space charge density profile. (*c*) Viscosity distribution profile. (*d*) Monomer density profile. (*e*) Counterion density profile. (*f*) Electric potential distribution profile. The PE solution consists of only one type of polymer, with $a = 1.0$ nm, $c_b = 0.1$ M, $f = 0.5$, $N_p = 200$, $D = 0.2$ nm, and H varies among 2, 3, 4, 5, 6 and 7 nm.

significantly reduced confinement (Alizadeh *et al.* 2021). Here, cases both with and without confinement effect are studied for comprehensive assessment.

Figure 13(*a*) plots the EOF velocity profiles for various $2H\kappa$ values. We can observe that the EOF follows a two-stage change. At the first stage, when the confinement effect is pronounced (i.e. $2H\kappa < 5$), the EOF exhibits a parabolic-like shape and rises to a higher peak with increasing $2H\kappa$. This peak is maximised at $2H\kappa = 4$, and at the second stage, when the confinement effect becomes weaker ($2H\kappa > 5$), the EOF shifts to a W-like shape, and the profile becomes gradually independent of $2H\kappa$. This variation of $v_x(z)$ is attributed to the combined influence of $\rho(z)$ and $\eta(z)$ as depicted in figures 13(*b*) and 13(*c*), respectively. From figures 13(*d*) and 13(*e*), we can observe that at the first stage under extreme confinement ($2H\kappa = 2$), $\phi^2(z)$ and $c_+(z)$ exhibits unique profiles. Specifically, polyanions are less depleted, while counterions are more significantly depleted near the surface wall compared to conditions with weaker confinement. Both $\phi^2(z)$ and $c_+(z)$ rise much more gradually to peak values smaller their respective bulk values at the centre of the nanochannel. As $2H\kappa$ increases, the depletion depth of both $\phi^2(z)$ and $c_+(z)$ remains nearly unchanged, and both $\phi^2(z)$ and $c_+(z)$ rise to absorption peaks larger than their respective bulk values. In the second stage, the profiles of $\phi^2(z)$ and $c_+(z)$ become independent of $2H\kappa$ when confinement is relatively weak.

Therefore, with the increase of $2H\kappa$, we observe that the profile of net charge density ρ and local viscosity $\eta(z)$ exhibits a trend similar to that of the monomer concentration $\phi^2(z)$ (figure 13*b*,*c*). It is noted that at high $2H\kappa$, when the confinement effect is weak, there exists a minor oscillation of net charge density in the near region of the nanochannel

https://doi.org/10.1017/jfm.2025.10181 Published online by Cambridge University Press

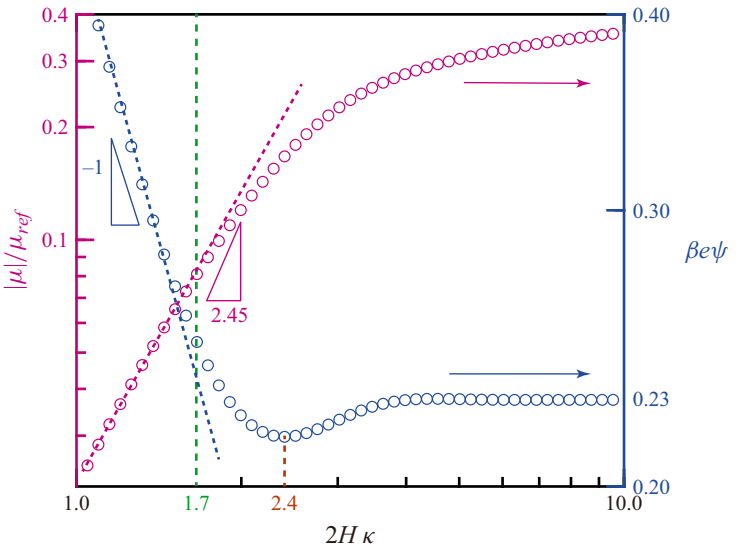


Figure 14. Reduced electro-osmotic mobility and non-dimensional induced zeta potential as a function of nanochannel height H.

centre, which gives rise to the W-like shape EOF (figure 13a). From figure 13(f), we can find that as $2H\kappa$ increases, the profile of $\beta e\psi$ becomes gradually independent, and an overcharging potential is observed under weak confinement.

Figure 14 plots how μ_{eof} and ψ vary with $H\kappa$. Applying the same processing method to the data as before, we can observe that when the confinement effect is strong ($2H\kappa < 1.7$), two scaling laws, $\mu_{eof} \propto (H\kappa)^{2.45}$ and $\psi \propto (H\kappa)^{-1}$, are reported. As $2H\kappa$ increases further, μ_{eof} rises more gradually, and is predicted to converge to its bulk value when $2H\kappa \to \infty$. Additionally, ψ first minimises at $2H\kappa = 2.4$, and converges to approximately 0.23 when $2H\kappa = 4$.

3.3. *The EOF in nanochannels with various wall effects*

In this subsection, we investigate the influence of wall effects on EOF through parametric studies. Three types of effects associated with the channel walls have been taken into account, namely the wall adsorption/depletion (characterised by adsorption length D), wall charge (characterised by surface charge density σ) and wall slip (characterised by slip length L_s).

3.3.1. *Effect of wall adsorption length on EOF*

We first probe into the effect of the van der Waals interactions between PEs and the surface walls on the EOF. As is discussed before, D is the adsorption parameter of the PEs and is inversely proportional to the van der Waals interactions. This indicates that when $D > 0$, the depletion of PEs near the wall becomes more pronounced as D approaches 0. Conversely, when $D < 0$, the adsorption of PEs onto the surface wall continues to increase. Notably, as $D \to \infty$, the van der Waals interaction between surface walls and PEs diminishes. In this subsubsection, both absorption ($D = 0.4$, 0.6, 0.8 nm) and depletion ($D = -0.4$, -0.6, -0.8 nm) cases are considered for comparative study.

Figure 15 depicts the physical characteristics of the EOF system under various D values. An evident influence of D can be observed in the absence of electrostatic interactions between the surface walls and the PE solutions (i.e. $\sigma = 0$). When the surface is attractive

https://doi.org/10.1017/jfm.2025.10181 Published online by Cambridge University Press

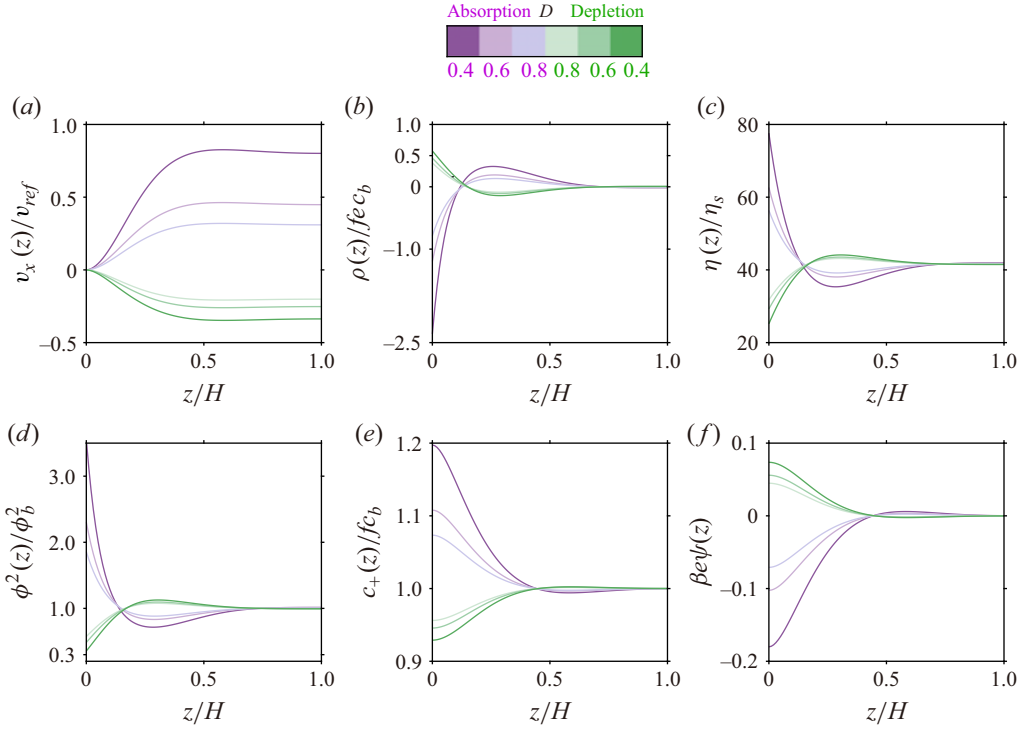


Figure 15. Dependence of EOF on absorption length D. (*a*) The EOF velocity profile. (*b*) Space charge density profile. (*c*) Viscosity distribution profile. (*d*) Monomer density profile. (*e*) Counterion density profile. (*f*) Electric potential distribution profile. The PE solution consists of only one type of polymer, with $a = 0.5$ nm, $c_b = 0.1$ M, $f = 0.5$, $N_p = 200$, $H = 5$ nm, and D varies among -0.4, -0.6, -0.8, 0.8, 0.6 and 0.4 nm.

($D < 0$), an EOF is generated in the positive x direction, whereas it flows in the opposite direction when the surface is repulsive ($D > 0$; figure 15*a*). Regardless of whether the surface is attractive or repulsive, the EOF exhibits a plug-like profile that becomes more pronounced as van der Waals interactions are strengthened (i.e. $|1/D|$ becomes larger). This variation of $v_x(z)$ is attributed to the combined influence of $\rho(z)$ and $\eta(z)$ as depicted in figures 15(*b*) and 15(*c*), respectively.

For attractive cases, due to the absorption force from surface walls, PE monomers tend to accumulate near the surface, and an absorption layer of counterions is also observed owing to the electrostatic attractions from the enriched polyanions (figure 15*d*,*e*). The enrichment layer of PEs is much thicker than that of the counterions, giving rise to a relatively high negative net charge density ρ (figure 15*b* and an induced negative zeta potential (figure 15*f*) at the surface wall. We can also observe that $\eta(z)$ shares a profile similar to that of $\phi^2(z)$ (figure 15*c*). The monomer concentration is much higher than the bulk value, and results in the increased viscosity based on (3.3). Conversely, for repulsive cases, profiles of all physical parameters undergo a reversal trend. Monomers and counterions are depleted to distinct degrees (figure 15*d*,*e*), and a positive net charge density can be observed in the vicinity of the surface wall (figure 15*b*). Whether the surface is attractive ($D < 0$) or repulsive ($D > 0$), a clear oscillation in net charge density ρ with a decaying amplitude is observed along the z axis. The local viscosity also shares a similar profile with $\phi^2(z)$, and a positive zeta potential is induced at the surface wall when $D > 0$ (figure 15*c*,*f*). Furthermore, when the van der Waals forces are intensified (i.e. $|1/D|$ becomes larger), all the physical quantities tend to deviate more from their respective bulk values. However,

https://doi.org/10.1017/jfm.2025.10181 Published online by Cambridge University Press

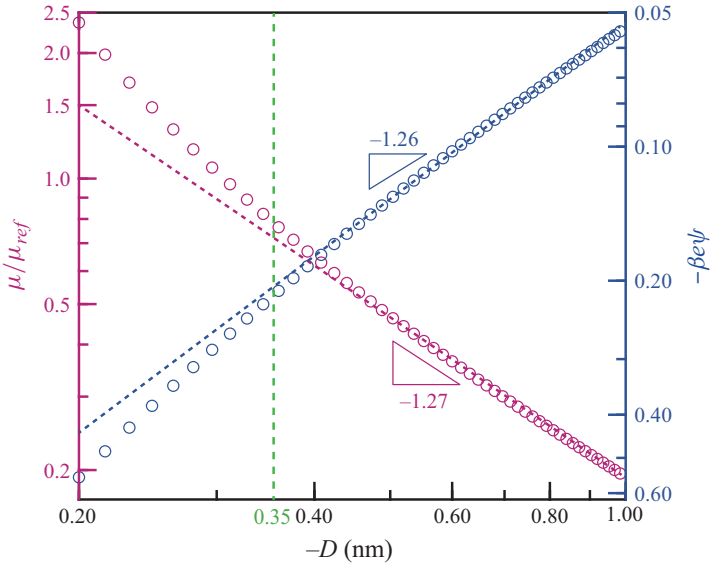


Figure 16. Reduced electro-osmotic mobility and non-dimensional induced zeta potential as functions of adsorption length D, when $D < 0$.

the sign of D wields a considerable influence on the system, despite its magnitude. It can be observed from figure 15(a) that for the same magnitude of D, the magnitude of EOF for attractive cases is nearly twice that of repulsive ones. This can be ascribed to the fact that although the viscous effect is more pronounced when $D < 0$ (figure 15c), it is compensated by the largely enhanced electric driving force (figure 15b), and results in the enhanced EOF demonstrated in figure 15(a).

Figures 16 and 17 plot how μ_{eof} and ψ vary with D. We can observe that the magnitudes of μ_{eof} and ψ decline under weakened van der Waals interactions. Applying the same processing method to the data as before, it can be illustrated that when the surface walls are adsorptive of PEs (i.e. $D < 0$) and the magnitude of adsorption effect is relatively weak ($D < -0.45$ nm), two scaling laws, $\mu_{eof} \propto D^{-1.27}$ and $\psi \propto D^{-1.26}$, are reported. When the surface walls are repulsive of PEs (i.e. $D > 0$) and the magnitude of depletion effect is relatively weak ($D > 0.44$ nm), two scaling laws, $\mu_{eof} \propto D^{-0.78}$ and $\psi \propto D^{-0.77}$, are reported.

3.3.2. *Effect of electrostatic force on EOF*

Our previous studies have focused primarily on the EOF behaviour of PE solutions in confined nanochannels with uncharged walls (i.e. $\sigma = 0$), and systematically investigated the impact of various parameters (e.g. c_b, f, H, D). In all the above cases, the surface walls carry no charge and exert no electrostatic force on polyanions and counterions in PE solutions. Hence for comparison and completeness, we examine how surface charge density σ affects the EOF of salt-free semi-dilute PE solutions. Unlike the van der Waals force, the surface walls can generate electrostatic interactions with charged ions through the Coulomb effect. In this subsubsection, cases when surface walls are both negatively charged ($\sigma = -0.1, -1, -10$ mC m^{-2}) and positively charged ($\sigma = 0.1, 1, 10$ mC m^{-2}) are considered for comprehensive assessment.

For positively charged cases, figure 18(a) illustrates that EOF is generated in the opposite x direction, the same as neutral cases. When the surface charge density is low

https://doi.org/10.1017/jfm.2025.10181 Published online by Cambridge University Press

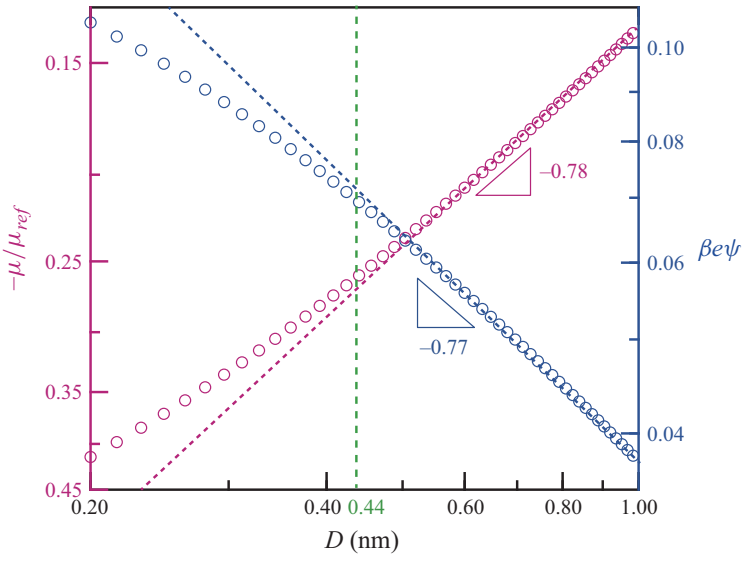


Figure 17. Reduced electro-osmotic mobility and non-dimensional induced zeta potential as functions of adsorption length D, when $D > 0$.

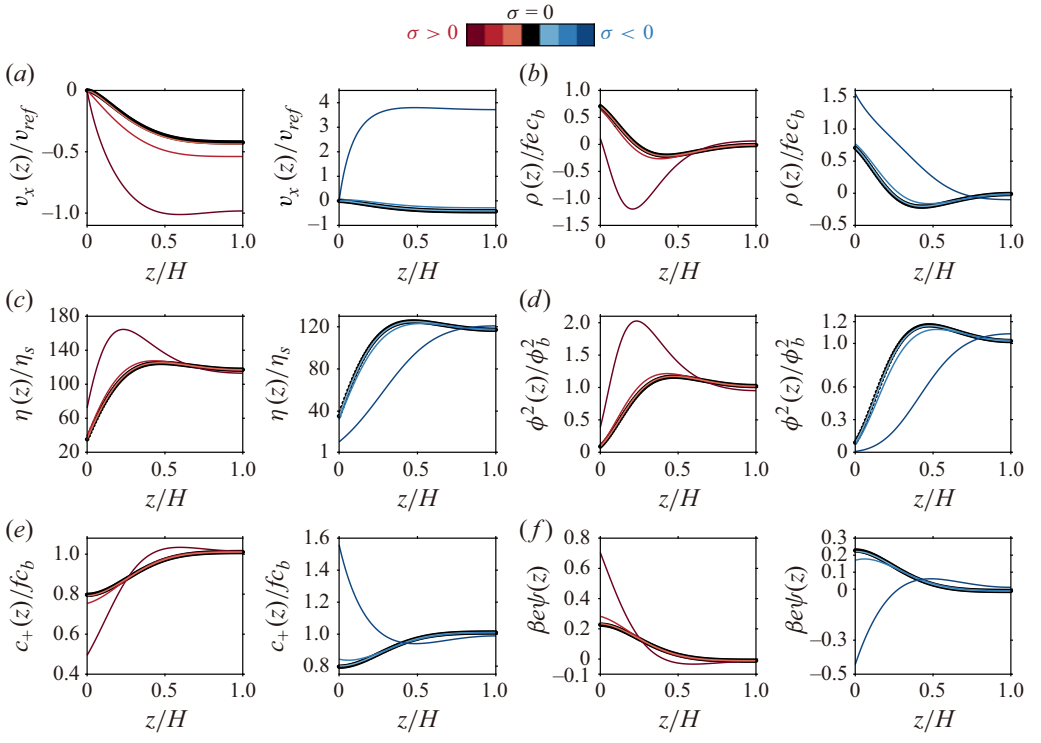


Figure 18. Dependence of EOF on surface charge density σ. (*a*) The EOF velocity profiles. (*b*) Space charge density profiles. (*c*) Viscosity distribution profiles. (*d*) Monomer density profiles. (*e*) Counterion density profiles. (*f*) Electric potential distribution profiles. The PE solution consists of only one type of polymer, with $a = 1.0$ nm, $c_b = 0.1$ M, $f = 0.5$, $N_p = 200$, $H = 5$ nm, $D = 0.2$ nm, and σ varies among -0.1, -1, -10, 0.1, 1, 10 mC m^{-2}.

https://doi.org/10.1017/jfm.2025.10181 Published online by Cambridge University Press

($\sigma \sim O(0.1\ \mathrm{mC\,m^{-2}})$), the generated EOF almost overlaps with that of the neutral case, which implies that the EOF is scarcely enhanced. As σ increases, the EOF becomes noticeably amplified compared to the neutral case. This augmentation intensifies with increasing σ, and can nearly double at $\sigma = 10\ \mathrm{mC\,m^{-2}}$. This variation of $v_x(z)$ is attributed to the combined influence of $\rho(z)$ and $\eta(z)$ as depicted in figure 18(*b*) and 18(*c*), respectively. As σ increases, polyanions become less depleted near the surface wall due to the electrostatic attraction from counterions on the slit surface. Consequently, $\phi^2(z)$ rises more rapidly, reaching a higher adsorption peak at a closer distance from the wall (figure 18*d*). When $\sigma = 10\ \mathrm{mC\,m^{-2}}$, this peak concentration can even reach twice the bulk value. Meanwhile, as the surface wall carries a higher density of positive charge, small counterions of similar charge released from the PEs become more depleted near the surface wall due to electrostatic repulsion (figure 18*e*). This variation in the concentration of charged carriers in the PE solution results in changes to the local net charge density $\rho(z)$. It can be observed that as σ increases, the net positive ρ near the surface wall becomes gradually diluted, with a larger portion of the nanochannel dominated by net negative charge (figure 18*b*). Specifically, when σ reaches $10\ \mathrm{mC\,m^{-2}}$, the EDL is almost occupied by net negative charge and the oscillation of ρ nearly vanishes. Hence with the increase of σ, more negative charges are dominant in the entire nanochannel, providing a stronger negative electric body force. However, this stronger body force is largely balanced by the increasing hindrance from viscosity as we can observe that $\eta(z)$ shares a profile similar to that of $\phi^2(z)$ (figure 18*c*). The competition effect between the driving electric force and the viscous effect gives rise to the nonlinear variation of μ_{eof} as depicted in figure 19. We also discover that when the surface walls carry more positive charge, zeta potential at the surface ψ exhibits a nonlinear variation with σ (figure 19) and an obvious overcharging potential is observed at $\sigma = 10\ \mathrm{mC\,m^{-2}}$.

However, things differ when surface walls are negatively charged. For simplicity, the increase of σ refers to the augmentation of the magnitude of the surface charge density. From figure 18(*a*), we can observe that the EOF initially weakens in the same direction as in the neutral case, and shifts to the positive x direction with increasing σ. At $\sigma = -10\ \mathrm{mC\,m^{-2}}$, the magnitude of EOF can be intensified to nearly eight times that of the neutral case. More interestingly, we discover that when σ reaches $-1\ \mathrm{mC\,m^{-2}}$, flows in the positive and opposite x direction coexist in the EOF; the sign of $v_x(z)$ reverses at $z \approx 2$ nm. This variation of $v_x(z)$ is attributed to the combined influence of $\rho(z)$ and $\eta(z)$ as depicted in figures 18(*b*) and 18(*c*), respectively. Figure 18(*d*) illustrates that when surface walls carry more negative charge, polyanions are more depleted, and $\phi^2(z)$ rises more gradually to a decaying absorption peak due to electrostatic repulsion from the slit walls. Notably, the adsorption peak nearly vanishes when the magnitude of σ is relatively high. In contrast, small counterions are more attracted to the oppositely charged surface wall, and when σ reaches $\sigma = -10\ \mathrm{mC\,m^{-2}}$, an enrichment layer forms at the surface (figure 18*e*). This variation in the concentration of charged carriers in the EDL leads to a broader distribution of net positive charge within the EDL, resulting in a stronger positive electric body force; an enrichment layer forms at the surface in the EDL (figure 18*b*), and accounts for the coexistence of two directions of flow. As surface charge density increases further, the EOF eventually reverses. Simultaneously, as $\eta(z)$ declines due to more depleted polyanions (figure 18*c*), the EOF is further strengthened, which results in the much more pronounced enhancement compared to positive cases. Figure 18(*f*) demonstrates that the zeta potential at the surface shifts to negative with increasing σ, and an obvious overcharging potential is observed at $\sigma = -10\ \mathrm{mC\,m^{-2}}$. Figure 20 illustrates that the magnitude of μ_{eof} first declines until it vanishes at $\sigma \approx -2\ \mathrm{mC\,m^{-2}}$,

https://doi.org/10.1017/jfm.2025.10181 Published online by Cambridge University Press

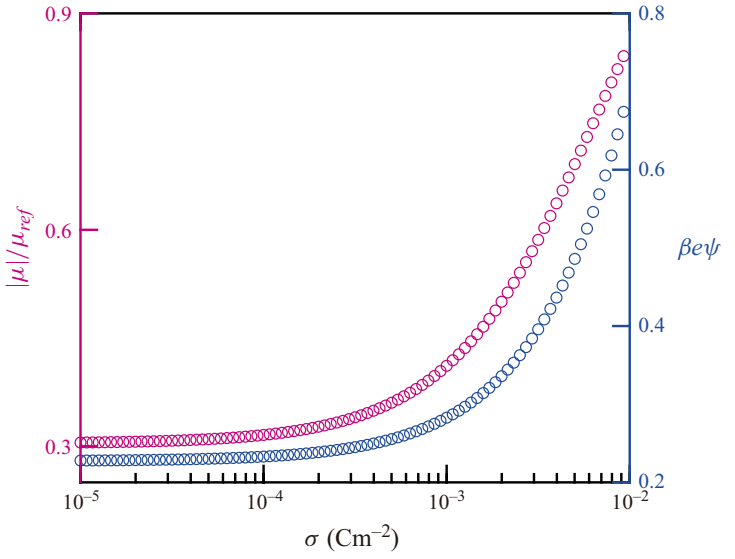


Figure 19. Reduced electro-osmotic mobility and non-dimensional zeta potential as functions of surface charge density σ, when $\sigma > 0$.

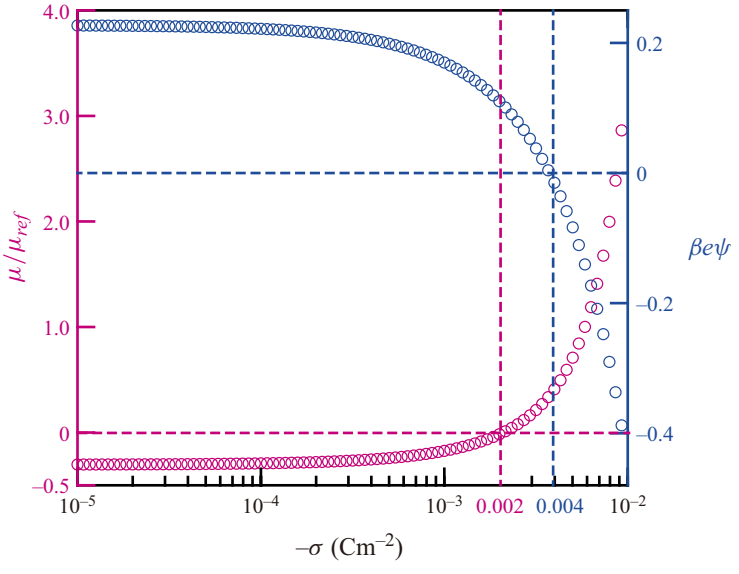


Figure 20. Reduced electro-osmotic mobility and non-dimensional zeta potential as functions of surface charge density σ, when $\sigma < 0$.

and then increases rapidly at higher σ. Also, ψ undergoes a nonlinear variation with σ. Interestingly, ψ reverses later than μ_{eof}, at $\sigma \approx -4$ mC m^{-2}.

3.3.3. *Co-action of wall effects on EOF*

Finally, we discuss the coupling effects of various wall interactions on the EOF. Figure 20 shows that for negatively charged walls, there is a specific surface charge density σ_z at which EOF mobility becomes zero. When the surface charge density exceeds this value,

https://doi.org/10.1017/jfm.2025.10181 Published online by Cambridge University Press

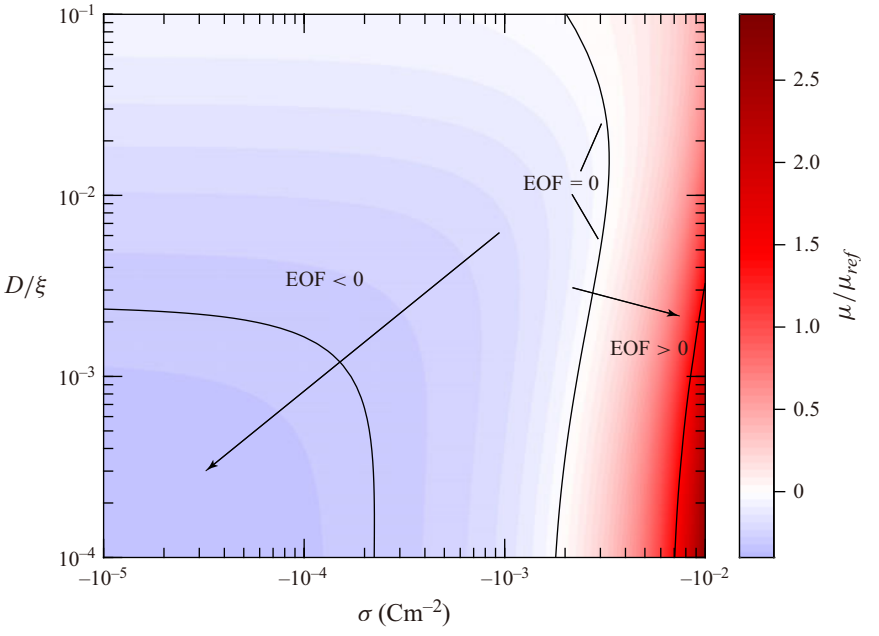


Figure 21. Heat map of reduced electro-osmotic mobility as a function of surface charge density σ and adsorption length D, when $\sigma < 0$ and $D > 0$.

the direction of EOF mobility reverses. Here, we further explore the impact of other wall interactions on this intriguing reversal phenomenon, and analyse the coupling effects of these interactions.

First, we take into account the influence of D. From our previous discussions about the impact of parameter D (i.e. the adsorption length) on EOF, we can see that when the walls are uncharged, the van der Waals forces exerted by the walls on the solution have a significant impact on both the direction and magnitude of EOF. It is noted here that although cases of uncharged adsorptive walls ($D < 0$) have also been taken into account, surface walls temd to exhibit a predominantly repulsive interaction with PE solutions (i.e. $D > 0$) in reality. Figure 21 illustrates the variation in the EOF mobility under the coupled effect of the wall's van der Waals repulsion and electrostatic repulsion. It can be observed that when D and σ change simultaneously, as predicted, there exists a distinct boundary line that reduces the EOF mobility (μ_{eof}) to zero. This zero line indicates that the critical EOF reversal surface charge density σ_z changes non-monotonically with the depletion length D. We can observe that at low D when the surface wall exerts a strong van der Waals force on PE solutions, σ_z increases with D and reaches its maximum at approximately $D/\xi = 0.01$. Subsequently, as the van der Waals repulsion gradually decreases, σ_z paradoxically decreases with an increase in D. Additionally, figure 21 illustrates that when μ_{eof} is negative, the effect of D on EOF is much more pronounced, as evidenced by the EOF contour lines. Conversely, when σ exceeds σ_z when EOF reverses, D gradually has a marginal impact on EOF. Within this range, electrostatic interactions play a dominant role, and we can discover that the EOF mobility rapidly increases with increasing σ.

Finally, we discuss the impact of wall slip effects. The slip effect is a complex phenomenon that can be viewed as a type of wall interaction. Its physical mechanism is intricate, and may involve various factors, such as wall adhesion, surface roughness

https://doi.org/10.1017/jfm.2025.10181 Published online by Cambridge University Press

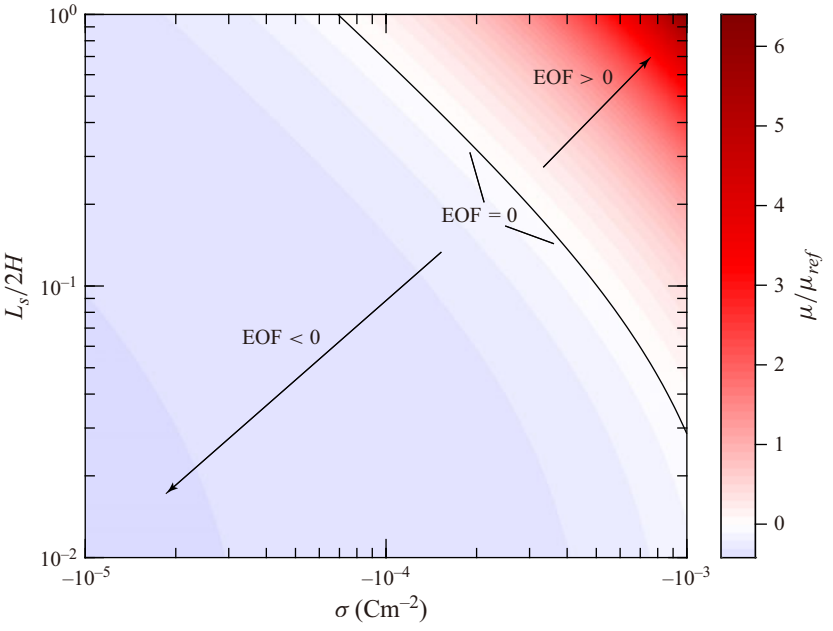


Figure 22. Heat map of reduced electro-osmotic mobility as a function of surface charge density σ and slip length L_s, when $\sigma < 0$.

and wettability. Here, we do not focus on the underlying physical mechanisms of the slip effect, but instead concentrate on the slip length L_s, which characterises the strength of the slip effect. It is noted that in the nanoslit system that we considered, the magnitude of L_s considered here is constrained to 0.1–10 nm, corresponding to dimensionless magnitude $L_s/2H$ in the range $0.01-1$. From figure 22, we can observe that the impact of L on σ_z is quite significant. As the slip effect becomes more pronounced, the EOF mobility reverses even at very low surface charge densities. Simultaneously, it can be observed that when σ is fixed, with the increase of slip length, EOF mobility gradually transits from negative to zero, then quickly evolves towards a positive direction.

4. Conclusions and outlook

In this work, we formulate a theoretical model for the EOF of semi-dilute polyelectrolyte (PE) solutions in slit nanochannels, and systematically investigate how various influencing factors affect the EOF. The theoretical model of EOF combines well-recognised mean-field theories of EDL and viscous properties of PE solutions, and the validity of the model is confirmed with the existing experiments. We find that when confined by the nanochannel, the structure of PE solutions exhibits unique properties due to the complex interplay between electrostatic interactions, excluded volume forces, EDL overlap and wall effects. The unique properties of confined PE solutions give rise to the nature of the EOF being influenced by multiple factors, making the EOF of the PE solution significantly different from that of a simple electrolyte solution.

First, we observe that a considerable EOF of PE solutions can be generated in the uncharged nanochannel due to a non-zero charge density originating from the complex interplay of PE solutions properties as well as multiple interactions. Such an EOF is controlled by both the electric body forces and the non-uniform viscosity distribution. We then conduct a systematic study on the influence of various parameters on this

https://doi.org/10.1017/jfm.2025.10181 Published online by Cambridge University Press

counterintuitive EOF. We reveal that the EOF mobility exhibits a non-monotonic change with monomer bulk concentration due to counteraction between electric body force and viscous hindrance; the charge fraction of the PEs has a complex and nonlinear effect on the EOF mobility in PE solutions; the EOF mobility exhibits a nonlinear decline for small charge fractions and tends to decrease consistently with the charge fraction for strongly charged cases; the EOF mobility exhibits a scaling law relationship with Kuhn length of polymer monomers and the polymerisation degree of a polymer chain and two scaling laws, $\mu_{eof} \propto a^{-0.44}$ and $\mu_{eof} \propto N_p^{-1}$, are reported; as channel height increases, the EOF profile shifts from the parabolic-like shape to W-shape, and eventually converges to the shape under unconfined conditions, where the EDLs do not overlap.

Second, we investigate the influence of three wall effects, namely adsorption length, surface charge density and slip length on the EOF. We discover that when the surface charge is absent, both the magnitude and direction of EOF are significantly influenced by the adsorption length, while the slip length has no effect. When the wall becomes increasingly charged, the influence of the surface charge density and the slip length on the EOF dominates, whereas that of adsorption length becomes marginal. We also reveal that when the surface wall is oppositely charged to polymer monomers, the EOF mobility extends a nonlinear variation with the surface charge density, while a zero net EOF followed by a mobility reversal is discovered when the surface wall is likely charged to polymer monomers. In the end, we demonstrate that the EOF is affected by various wall effects jointly in a complicated manner by analysing the reversal point of EOF mobility.

This study combines a mean-field EDL theory with a mean-field viscosity model of the semi-dilute PE solution to investigate the EOF of the PE solution in slit nanochannels. Our work can provide a useful reference for studying the EOF of complex fluids. However, we acknowledge that our work focused on only the case of one-dimensional channels with walls of idealised properties, and the model of PE viscosity ina nanochannel still requires improvement since we have not taken shear effects into account. Therefore, more efforts are required to investigate the EOF behaviour of PE solutions in more realistic systems with higher accuracy. In future research, we recommend exploring more complex PE solution systems under various confinement conditions, and utilising more advanced EDL models (such as classic DFT (density functional theory)) and viscosity models (shear-rate dependence) to develop more accurate EOF models. Meanwhile, relevant experiments, such as nanoscale particle image velocimetry and state-of-the-art small flow rate measurement, are expected to be carried out to validate the theory and confirm the prediction.

Acknowledgements. We acknowledge fruitful discussion on the EDL with J. Jiang fromthe Institute of Chemistry, Chinese Academy of Sciences, on the rheology properties of PE solutions with G. Chen from Peking Unversity, and on the EOF with Y. Uematsu from Kyushu Institute of Technology.

Funding. This work was supported by the National Natural Science Foundation of China (grant no. 51976157) and the Fundamental Research Funds for Central Universities.

Declaration of interests. The authors report no conflict of interest.

Data availability statement. The data that support the findings of this study are available from the corresponding author upon reasonable request.

Author contributions. C.Z. and X.L. conceived the idea and designed the algorithm; W.Z. provided theoretical supports; X.L. performed calculations and data analysis; X.L and W.Z. performed visualisation; X.L. wrote the manuscript; W.Z. and C.Z. reviewed and polished the manuscript; K.J., Q.W. and C.Z. discussed the results and provided constructive comments on the manuscript.

https://doi.org/10.1017/jfm.2025.10181 Published online by Cambridge University Press

Appendix A. Derivation of the governing equations with the variational method

First, the variational method is applied to $\mathcal{F} = \mathcal{F}_p(z) + \mathcal{F}_i(z) + \mathcal{F}_c(z)$ with respect to $\phi(z)$. Noting that the chemical potential is taken as $\mu_p = \nu\phi_b^2/\beta$ (De Gennes 1982), and $\phi(z)$ exists only in the $\mathcal{F}_p(z)$ and $\mathcal{F}_c(z)$, we can obtain

$$-\frac{a^2}{3}\frac{\mathrm{d}^2\phi}{\mathrm{d}z^2} + 2\nu(\phi^3(z)) - 2\phi_b^2\,\phi(z) - 2\beta e f\psi\,\phi(z) = 0. \tag{A1}$$

Then the governing equation for $\phi(z)$ can be derived as

$$\frac{a^2}{6}\frac{\mathrm{d}^2\phi}{\mathrm{d}z^2} = \nu\phi\left(\phi^2 - \phi_b^2\right) - f\phi\beta e\psi, \tag{A2}$$

which is the so-called Edward equation (Uematsu & Araki 2013).

Similarly, applying the variational method to $\mathcal{F} = \mathcal{F}_p(z) + \mathcal{F}_i(z) + \mathcal{F}_c(z)$ with respect to $c_+(z)$ and $c_-(z)$, and noting that the chemical potentials of small ions are taken as $\mu_{i=+/-} = \ln c_i/\beta$ (Borukhov *et al.* 1998), we can obtain

$$\ln(c_+(z)/c_{+,b}) + \beta e\psi = 0, \tag{A3}$$

$$\ln(c_-(z)/c_{-,b}) - \beta e\psi = 0, \tag{A4}$$

from which we can derive the expressions for $c_+(z)/c_{+,b}$ and $c_-(z)/c_{-,b}$ as (2.8) and (2.9).

Finally, the variational method is applied to $\mathcal{F} = \mathcal{F}_p(z) + \mathcal{F}_i(z) + \mathcal{F}_c(z)$ with respect to $\psi(z)$. In the resultant equation, substituting $c_+(z)$ and $c_-(z)$ with (A3) and (A4) respectively, we can derive the governing equation for $\psi(z)$ as (2.7), which is the modified Poisson–Boltzmann equation.

Appendix B. Validation of the mean-field EDL model via molecular dynamics simulation

We also perform a molecular dynamics (MD) simulation of coarse-grained PE solutions confined in neutral nanochannels to validate the mean-field model utilised in this work. The specific settings of the coarse-grained molecular simulation follow previous works (Ghelichi & Eikerling 2016; Bagchi & Olvera de la Cruz 2020; Bagchi, Nguyen & Olvera de la Cruz 2020; Radhakrishnan & Singh 2021; Liang & de Pablo 2022; Yu *et al.* 2022; Zhu, Luo & Paddison 2022) and will not be elaborated here.

Table 2 presents the key parameters and their values in the calculations. Values of the parameters in the MD simulation are set to be the same as those in our mean-field model. For MD simulations, two approaches (illustrated in figure 23*a*,*b*) have been utilised to describe the charge characteristics of the PE chains. In the first approach, each PE monomer on a PE chain (pink beads in figure 23*a*) is uniformly charged with $-0.5e$. In the second approach, one randomly chosen half of the total monomers on a PE chain are charged, with each monomer carrying $-e$ (red beads in figure 23*b*). These two approaches lead to a same charge fraction $f = 0.5$. The second approach is more like a real PE solution, and the first is a simplified model of the PE solution. The MD with the first approach is denoted as MD-UC (uniformly charged), and the MD with the second approach is denoted as MD-RC (randomly charged).

The concentration distributions of three charged species, i.e. cations, anions and polyions, across the channel EDL predicted with three methods are shown in figure 23(*c*).

https://doi.org/10.1017/jfm.2025.10181 Published online by Cambridge University Press

Parameters	a	f	N_p	c_s	c_b	D	ν	σ	H	T	ϵ
Values	0.65 nm	0.5	100	10 mM	95 mM	0.06 nm	0.05 nm^3	0 C m^{-2}	2 nm	300 K	80

Table 2. Values of key parameters used in the comparison.

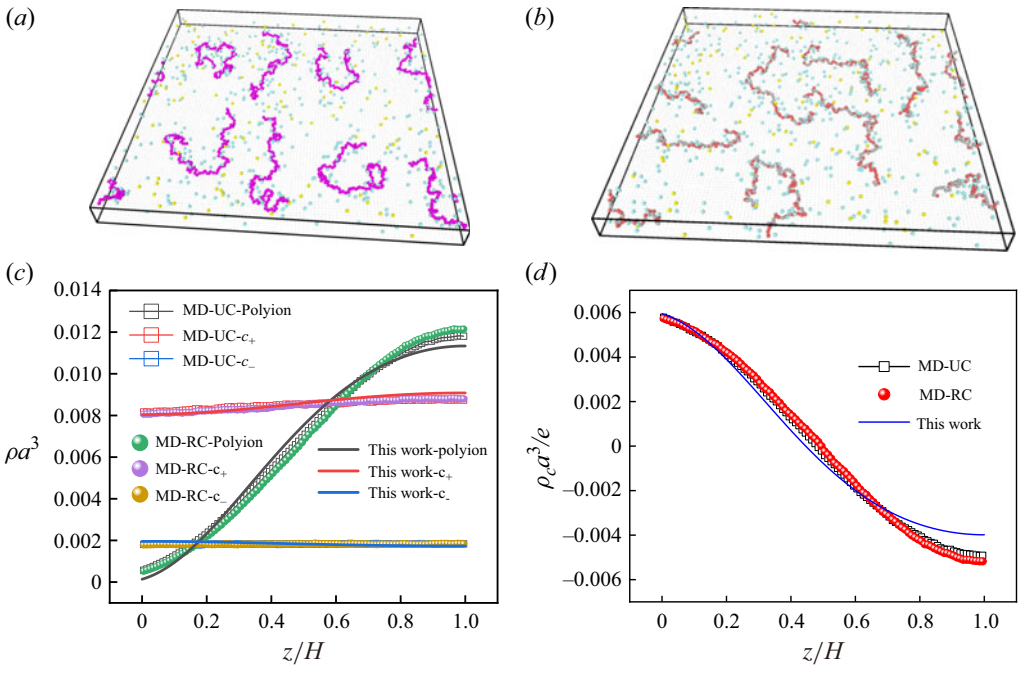


Figure 23. (*a*) Snapshot of PE solutions during MD simulation with uniform charges on the chains. Pink beads represent polyions, and each carries $-0.5e$ charge. Blue beads represent cations, and yellow beads represent anions. (*b*) Snapshot of PE solutions during MD simulation with random charges on the chains. Red beads represent polyions, and each carries $-e$ charge. Grey beads represent neutral monomers and have the same number as red beads, giving rise to charge fraction 0.5. Blue beads represent cations, and yellow beads represent anions. (*c*) Comparison of the EDL ion concentration distributions (polyions, cations and anions) across the channel obtained from two MD simulations and the mean-field model. (*d*) The net charge density distributions across the channel EDL calculated from the data in (*c*).

It is observed that MD-UC and MD-RC show very remarkable agreement, and the mean-field model in this work also agrees with the two MD simulations reasonably well. These results verify the rationality and reliability of the mean-field EDL model adopted in our study. Furthermore, the net charge density distribution across the channel EDL calculated from figure 23(*c*) is also shown in figure 23(*d*). The interaction of the net charge density and the external electric field induces the EOF observed in the current study.

References

ADACHI, Y. & XIAO, J. 2013 Initial stage of bridging flocculation of PSL particles induced by an addition of polyelectrolyte under high ionic strength. *Colloids Surf. A: Physicochem. Engng Aspects* **435**, 127–131.

AI, Y., YALCIN, S.E., GU, D., BAYSAL, O., BAUMGART, H., QIAN, S. & BESKOK, A. 2010 A low-voltage nano-porous electroosmotic pump. *J. Colloid Interface Sci.* **350** (2), 465–470.

ALIZADEH, A., HSU, W., WANG, M. & DAIGUJI, H. 2021 Electroosmotic flow: from microfluidics to nanofluidics. *Electrophoresis* **42** (7-8), 834–868.

https://doi.org/10.1017/jfm.2025.10181 Published online by Cambridge University Press

ALSHAWABKEH, A.N., YEUNG, A.T. & BRICKA, M.R. 1999 Practical aspects of in-situ electrokinetic extraction. *J. Environ. Engng* **125** (1), 27–35.

AZIZ, U.A., MUKARRAM, A. & KASHIF, A. 2020 Electroosmotic slip flow of Oldroyd-B fluid between two plates with non-singular kernel. *J. Comput. Appl. Maths* **376**, 112885.

BAGCHI, D., NGUYEN, T.D. & OLVERA DE LA CRUZ, M. 2020 Surface polarization effects in confined polyelectrolyte solutions. *Proc. Natl Acad. Sci. USA* **117** (33), 19677–19684.

BAGCHI, D. & OLVERA DE LA CRUZ, M. 2020 Dynamics of a driven confined polyelectrolyte solution. *J. Chem. Phys.* **153** (18), 184904.

BHAGAVATULA, N. & CASTRO, J.M. 2007 Modelling and experimental verification of pressure prediction in the in-mould coating (IMC) process for injection moulded parts. *Model. Simul. Mater. Sci. Engng* **15** (2), 171–189.

BHATTACHARYYA, S. & BAG, N. 2019 Enhanced electroosmotic flow and ion selectivity in a channel patterned with periodically arranged polyelectrolyte-filled grooves. *Microfluid. Nanofluid.* **23** (3), 46.

BHATTACHARYYA, S., ZHENG, Z. & CONLISK, A.T. 2005 Electro-osmotic flow in two-dimensional charged micro- and nanochannels. *J. Fluid Mech.* **540**, 247–267.

BISCOMBE, C.J.C. 2017 The discovery of electrokinetic phenomena: setting the record straight. *Angew. Chem. Intl Ed. Engl.* **56** (29), 8338–8340.

BONDAREV, D., MELNIKOV, S. & ZABOLOTSKIY, V. 2023 New homogeneous and bilayer anion-exchange membranes based on N,N-diallyl-N,N-dimethylammonium chloride and ethyl methacrylate copolymer. *J. Membr. Sci.* **675**, 121510.

BORUKHOV, I., ANDELMAN, D. & ORLAND, H. 1998 Random polyelectrolytes and polyampholytes in solution. *Eur. Phys. J. B* **5** (4–6), 869–880.

CARRILLO, J.-M.Y. & DOBRYNIN, A.V. 2011 Polyelectrolytes in salt solutions: molecular dynamics simulations. *Macromolecules* **44** (14), 5798–5816.

CARRILLO, J.M.Y. & DOBRYNIN, A.V. 2014 Salt effect on osmotic pressure of polyelectrolyte solutions: simulation study. *Polymers (Basel)* **6** (7), 1897–1913.

CHEN, D., LI, J., CHEN, H., ZHANG, L., ZHANG, H. & MA, Y. 2019 Electroosmotic flow behavior of viscoelastic LPTT fluid in a microchannel. *Micromachines (Basel)* **10** (12), 881.

CHEN, G., PERAZZO, A. & STONE, H.A. 2020 Influence of salt on the viscosity of polyelectrolyte solutions. *Phys. Rev. Lett.* **124** (17), 177801.

CHEN, G., PERAZZO, A. & STONE, H.A. 2021 Electrostatics, conformation, and rheology of unentangled semidilute polyelectrolyte solutions. *J. Rheo.* **65** (4), 507–526.

COMBET, J., LORCHAT, P. & RAWISO, M. 2012 Salt-free aqueous solutions of polyelectrolytes: small angle X-ray and neutron scattering characterization. *Eur. Phys. J. Special Topics* **213** (1), 243–265.

DAS, S. & CHAKRABORTY, S. 2006 Analytical solutions for velocity, temperature and concentration distribution in electroosmotic microchannel flows of a non-Newtonian bio-fluid. *Anal. Chim. Acta* **559** (1), 15–24.

DE GENNES, P.G. 1982 Polymers at an interface. *Macromolecules* **15** (2), 492–500.

DE GENNES, P.G., PINCUS, P., VELASCO, R.M. & BROCHARD, F. 1976 Remarks on polyelectrolyte conformation. *J. Phys.* **37** (12), 1461–1473.

DOBRYNIN, A.V. 2020 Polyelectrolytes: on the doorsteps of the second century. *Polymer* **202**, 122714.

DOBRYNIN, A.V., COLBY, R.H. & RUBINSTEIN, M. 1995 Scaling theory of polyelectrolyte solutions. *Macromolecules* **28** (6), 1859–1871.

DOBRYNIN, A.V. & RUBINSTEIN, M. 2005 Theory of polyelectrolytes in solutions and at surfaces. *Prog. Polym. Sci.* **30** (11), 1049–1118.

DUCHANOIS, R.M., EPSZTEIN, R., TRIVEDI, J.A. & ELIMELECH, M. 2019 Controlling pore structure of polyelectrolyte multilayer nanofiltration membranes by tuning polyelectrolyte-salt interactions. *J. Membr. Sci.* **581**, 413–420.

EL-SHEHAWY, E.F., EL-DABE, N.T. & EL-DESOKY, I.M. 2006 Slip effects on the peristaltic flow of a non-Newtonian Maxwellian fluid. *Acta Mechanica* **186** (1–4), 141–159.

FENG, H. & WONG, T. 2019 Net fluid flow and non-Newtonian effect in induced-charge electro-osmosis of polyelectrolyte solutions. *Phys. Rev. E* **100** (1), 013105.

FENG, H.C., HUANG, Y., WONG, T.N. & DUAN, F. 2017 Electrolyte effect in induced charge electroosmosis. *Soft Matt.* **13** (28), 4864–4870.

FERRÁS, L.L., NÓBREGA, J.M. & PINHO, F.T. 2012 Analytical solutions for Newtonian and inelastic non-Newtonian flows with wall slip. *J. Non-Newtonian Fluid Mech.* **175–176**, 76–88.

FUOSS, R.M. 1951 Polyelectrolytes. *Discuss. Faraday Soc.* **11**, 125–134.

GARTNER, T.E., III & JAYARAMAN, A. 2019 Modeling and simulations of polymers: a roadmap. *Macromolecules* **52** (3), 755–786.

https://doi.org/10.1017/jfm.2025.10181 Published online by Cambridge University Press

GHELICHI, M. & EIKERLING, M.H. 2016 Conformational properties of comb-like polyelectrolytes: a coarse-grained MD study. *J. Phys. Chem. B* **120** (10), 2859–2867.
GHIYA, N. & TIWARI, A. 2024 Unsteady electroosmotic flow of Carreau–Newtonian fluids through a cylindrical tube. *Intl J. Multiphase Flow* **179**, 104913.
GHOSH, U., CHAUDHURY, K. & CHAKRABORTY, S. 2016 Electroosmosis over non-uniformly charged surfaces: modified Smoluchowski slip velocity for second-order fluids. *J. Fluid Mech.* **809**, 664–690.
GUBBIOTTI, A., BALDELLI, M., DI MUCCIO, G., MALGARETTI, P., MARBACH, S. & CHINAPPI, M. 2022 Electroosmosis in nanopores: computational methods and technological applications. *Adv. Phys.* **7** (1), 2036638.
HAO, Y., TANG, L., PENG, L., LIU, R., ZHOU, T. & LI, J. 2024 Field effect control of ion transport in power-law fluids in a nanochannel. *Colloids Surf. A: Physicochem. Engng Aspects* **697**, 134475.
JI, J., QIAN, S. & LIU, Z. 2021 Electroosmotic flow of viscoelastic fluid through a constriction microchannel. *Micromachines (Basel)* **12** (4), 417.
JIANG, J. 2022 Software package: an advanced theoretical tool for inhomogeneous fluids (ATIF). *Chin. J. Polym. Sci.* **40** (2), 220–230.
JIANG, J., GINZBURG, V.V. & WANG, Z.G. 2018 Density functional theory for charged fluids. *Soft Matt.* **14** (28), 5878–5887.
JIANG, J., GINZBURG, V.V. & WANG, Z.G. 2019 On the origin of oscillatory interactions between surfaces mediated by polyelectrolyte solution. *J. Chem. Phys.* **151** (21), 214901.
JIAO, K., ZHANG, W., CHUAN, R., YAN, H., ZOU, A., WANG, Q., YANG, C. & ZHAO, C. 2022 Structural features and electrostatic energy storage of electric double layers in confined polyelectrolyte solutions under low-salt conditions. *Phys. Chem. Chem. Phys.* **24** (44), 27009–27022.
KARAN, P., CHAKRABORTY, J. & CHAKRABORTY, S. 2018 Electrokinetics over hydrophobic surfaces. *Electrophoresis* **40** (5), 616–624.
KO, C., LI, D., MALEKANFARD, A., WANG, Y., FU, L. & XUAN, X. 2019 Electroosmotic flow of non-Newtonian fluids in a constriction microchannel. *Electrophoresis* **40** (10), 1387–1394.
LI, F.Q. & JIAN, Y.J. 2019 Solute dispersion generated by alternating current electric field through polyelectrolyte-grafted nanochannel with interfacial slip. *Intl J. Heat Mass Transfer* **141**, 1066–1077.
LI, F.Q., JIAN, Y.J., CHANG, L., ZHAO, G.P. & YANG, L.G. 2016 Alternating current electroosmotic flow in polyelectrolyte-grafted nanochannel. *Colloids Surf. B* **147**, 234–241.
LI, Z. & WU, J. 2006 Density functional theory for polyelectrolytes near oppositely charged surfaces. *Phys. Rev. Lett.* **96** (4), 048302.
LIANG, H. & DE PABLO, J.J. 2022 A coarse-grained molecular dynamics study of strongly charged polyelectrolyte coacervates: interfacial, structural, and dynamical properties. *Macromolecules* **55** (10), 4146–4158.
LOPEZ, C.G. 2019 Entanglement properties of polyelectrolytes in salt-free and excess-salt solutions. *ACS Macro Lett.* **8** (8), 979–983.
LOPEZ, C.G., COLBY, R.H., GRAHAM, P. & CABRAL, J.T. 2017 Viscosity and scaling of semiflexible polyelectrolyte NaCMC in aqueous salt solutions. *Macromolecules* **50** (1), 332–338.
LOPEZ, C.G., ROGERS, S.E., COLBY, R.H., GRAHAM, P. & CABRAL, J.T. 2015 Structure of sodium carboxymethyl cellulose aqueous solutions: a SANS and rheology study. *J. Polym. Sci.* **53** (7), 492–501.
MA, D., SU, M., QIAN, J., WANG, Q., MENG, F., GE, X., YE, Y. & SONG, C. 2020 Heavy metal removal from sewage sludge under citric acid and electroosmotic leaching processes. *Separation Purif. Technol.* **242**, 116822.
MANNING, G.S. 1978 Molecular theory of polyelectrolyte solutions with applications to electrostatic properties of polynucleotides. *Q. Rev. Biophys.* **11** (2), 179–246.
MARTÍNEZ, L., BAUTISTA, O., ESCANDÓN, J. & MÉNDEZ, F. 2016 Electroosmotic flow of a Phan-Thien–Tanner fluid in a wavy-wall microchannel. *Colloids Surf. A: Physicochem. Engng Aspects* **498**, 7–19.
MATSUMOTO, A. 2022 Rheology of polyelectrolyte solutions: current understanding and perspectives. *Nihon Reoroji Gakkaishi* **50** (1), 43–50.
MISRA, J.C. & SINHA, A. 2015 Electro-osmotic flow and heat transfer of a non-Newtonian fluid in a hydrophobic microchannel with Navier slip. *J. Hydrodyn.* **27** (5), 647–657.
MONDAL, A. & SHIT, G.C. 2017 Transport of magneto-nanoparticles during electro-osmotic flow in a micro-tube in the presence of magnetic field for drug delivery application. *J. Magn. Magn. Mater.* **442**, 319–328.
MURTAZA, S., KUMAM, P., AHMAD, Z., SITTHITHAKERNGKIET, K. & ALI, I.E. 2022 Finite difference simulation of fractal-fractional model of electro-osmotic flow of Casson fluid in a micro channel. *IEEE Access* **10**, 26681–26692.
NAKAMURA, I. 2018 Effects of dielectric inhomogeneity and electrostatic correlation on the solvation energy of ions in liquids. *J. Phys. Chem. B* **122** (22), 6064–6071.

https://doi.org/10.1017/jfm.2025.10181 Published online by Cambridge University Press

NG, C. 2013 Combined pressure-driven and electroosmotic flow of Casson fluid through a slit microchannel. *J. Non-Newtonian Fluid Mech.* **198**, 1–9.

NG, C. & QI, C. 2014 Electroosmotic flow of a power-law fluid in a non-uniform microchannel. *J. Non-Newtonian Fluid Mech.* **208**, 118–125.

NIERLICH, M., BOUE, F., LAPP, A. & OBERTHÜR, R. 1985 Characteristic lengths and the structure of salt free polyelectrolyte solutions: a small angle neutron scattering study. *Colloid Polym. Sci.* **263** (12), 955–964.

NOREEN, S., WAHEED, S., HUSSANAN, A. & LU, D. 2019 Analytical solution for heat transfer in electroosmotic flow of a Carreau fluid in a wavy microchannel. *Appl. Sci.* **9** (20), 4359.

OLIVARES, M.L., VERA-CANDIOTI, L. & BERLI, C.L.A. 2009 The EOF of polymer solutions. *Electrophoresis* **30** (5), 921–928.

PANCHUN, L., SHAOWEI, W. & MOLI, Z. 2020 Numerical study of rotating electroosmotic flow of Oldroyd-B fluid in a microchannel with slip boundary condition. *Chin. J. Phys.* **65**, 459–471.

PEREZ OCAMPO, L., WEISS, L.B., JARDAT, M., LIKOS, C.N. & DAHIREL, V. 2022 Electroosmotic flow induced lift forces on polymer chains in nanochannels. *ACS Polym. Au* **2** (4), 245–256.

PODGORNIK, R. 1992 Self-consistent-field theory for confined polyelectrolyte chains. *J. Phys. Chem.* **96** (2), 884–896.

RADHAKRISHNAN, K. & SINGH, S.P. 2021 Collapse of a confined polyelectrolyte chain under an AC electric field. *Macromolecules* **54** (17), 7998–8007.

ROY, D., BHATTACHARJEE, S. & DE, S. 2020 Mass transfer of a neutral solute in polyelectrolyte grafted soft nanochannel with porous wall. *Electrophoresis* **41** (7–8), 578–587.

SARMA, R., DEKA, N., SARMA, K. & MONDAL, P.K. 2018 Electroosmotic flow of Phan-Thien–Tanner fluids at high zeta potentials: an exact analytical solution. *Phys. Fluids* **30** (6), 062001.

SHAFIR, A., ANDELMAN, D. & NETZ, R.R. 2003 Adsorption and depletion of polyelectrolytes from charged surfaces. *J. Phys. Chem.* **119** (4), 2355–2362.

SHEN, K., FAN, M. & HALL, L.M. 2021 Molecular dynamics simulations of ion-containing polymers using generic coarse-grained models. *Macromolecules* **54** (5), 2031–2052.

SHOJAEIAN, M. & KOŞAR, A. 2014 Convective heat transfer and entropy generation analysis on Newtonian and non-Newtonian fluid flows between parallel-plates under slip boundary conditions. *Intl J. Heat Mass Transfer* **70**, 664–673.

SIRIA, A., BOCQUET, M. & BOCQUET, L. 2017 New avenues for the large-scale harvesting of blue energy. *Nat. Rev. Chem.* **1** (11), 0091.

SIVASANKAR, V., ETHA, S., SACHAR, H. & DAS, S. 2021 Thermo-osmotic transport in nanochannels grafted with pH-responsive polyelectrolyte brushes modelled using augmented strong stretching theory. *J. Fluid Mech.* **917**, A31.

SQUIRES, T.M. & BAZANT, M.Z. 2006 Breaking symmetries in induced-charge electro-osmosis and electrophoresis. *J. Fluid Mech.* **560**, 65–101.

SRIVALLY, A. & REZA, M. 2023 Analytical solution for electroosmotic flow of Casson fluid in varying microchannel with zeta potential. *J. Central South Univ.* **30** (8), 2627–2641.

VANDER STRAETEN, A., BRATEK-SKICKI, A., GERMAIN, L., D'HAESE, C., ELOY, P., FUSTIN, C.A. & DUPONT-GILLAIN, C. 2017 Protein-polyelectrolyte complexes to improve the biological activity of proteins in layer-by-layer assemblies. *Nanoscale* **9** (44), 17186–17192.

TALEBI, R., ASHRAFIZADEH, S.N. & SADEGHI, A. 2021 Hydrodynamic dispersion by electroosmotic flow in soft microchannels: consideration of different properties for electrolyte and polyelectrolyte layer. *Chem. Engng Sci.* **229**, 116058.

TANG, G., LI, X., HE, Y. & TAO, W. 2009 Electroosmotic flow of non-Newtonian fluid in microchannels. *J. Non-Newtonian Fluid Mech.* **157** (1–2), 133–137.

UEMATSU, Y. 2015 Nonlinear electro-osmosis of dilute non-adsorbing polymer solutions with low ionic strength. *Soft Matt.* **11** (37), 7402–7411.

UEMATSU, Y. & ARAKI, T. 2013 Electro-osmotic flow of semidilute polyelectrolyte solutions. *J. Chem. Phys.* **139** (9), 094901.

ÜZÜM, C., CHRISTAU, S. & VON KLITZING, R. 2011 Structuring of polyelectrolyte (NaPSS) solutions in bulk and under confinement as a function of concentration and molecular weight. *Macromolecules* **44** (19), 7782–7791.

ÜZÜM, C., MAKUSKA, R. & VON KLITZING, R. 2012 Effect of molecular architecture on the polyelectrolyte structuring under confinement. *Macromolecules* **45** (7), 3168–3176.

VARONGCHAYAKUL, N., HUTTNER, D., GRINSTAFF, M.W. & MELLER, A. 2018 Sensing native protein solution structures using a solid-state nanopore: unraveling the states of VEGF. *Sci. Rep. UK* **8** (1), 1017.

VLASSIOUK, I., SMIRNOV, S. & SIWY, Z. 2008 Ionic selectivity of single nanochannels. *Nano Lett.* **8** (7), 1978–1985.

https://doi.org/10.1017/jfm.2025.10181 Published online by Cambridge University Press

WOODWARD, C.E. & JONSSON, B. 1991 Monte-Carlo and mean field studies of a polyelectrolyte in salt solution. *Chem. Phys.* **155** (2), 207–219.

XU, Y., NAZEER, M., HUSSAIN, F., KHAN, M.I., HAMEED, M., SHAH, N.A. & CHUNG, J.D. 2021 Electro-osmotic flow of biological fluid in divergent channel: drug therapy in compressed capillaries. *Sci. Rep. UK* **11** (1), 23652.

YETHIRAJ, A. 2009 Liquid state theory of polyelectrolyte solutions. *J. Phys. Chem. B* **113** (6), 1539–1551.

YU, B., LIANG, H., RUMYANTSEV, A.M. & DE PABLO, J.J. 2022 Isotropic-to-nematic transition in salt-free polyelectrolyte coacervates from coarse-grained simulations. *Macromolecules* **55** (21), 9627–9639.

ZHAO, C. & YANG, C. 2012 Advances in electrokinetics and their applications in micro/nano fluidics. *Microfluid. Nanofluid.* **13** (2), 179–203.

ZHAO, C. & YANG, C. 2013 Electrokinetics of non-Newtonian fluids: a review. *Adv. Colloid Interface Sci.* **201**, 94–108.

ZHAO, C., ZHOLKOVSKIJ, E., MASLIYAH, J.H. & YANG, C. 2008 Analysis of electroosmotic flow of power-law fluids in a slit microchannel. *J. Colloid Interface Sci.* **326** (2), 503–510.

ZHU, Z., LUO, X. & PADDISON, S.J. 2022 Coarse-grained modeling of ion-containing polymers. *Chem. Rev.* **122** (12), 10710–10745.

https://doi.org/10.1017/jfm.2025.10181 Published online by Cambridge University Press